Short-term oscillation and falling dynamics for a water drop dripping in quiescent air

B. Zhang and Y. Ling[*]

Department of Mechanical Engineering, Baylor University, Texas 76798, USA

P.-H. Tsai and A.-B. Wang[†]

Institute of Applied Mechanics, National Taiwan University, Taipei, 10617, Taiwan, Republic of China

S. Popinet and S. Zaleski

Sorbonne Universités and CNRS, Institut Jean le Rond d'Alembert, UMR 7190, F-75005, Paris, France

The short-term transient falling dynamics of a dripping water drop in quiescent air has been investigated through both simulation and experiment. A representative case with a low inflow rate in the dripping regime is considered. The focus is on the short-term behavior and the time range considered covers about eight dominant second-mode oscillations of the drop after it is formed. Due to the small fluid inertia at the inlet, the growth of the drop is quasistatic and is well captured by the static pendant drop theory. Nevertheless, it is demonstrated that the pinching dynamics and the resulting postformation state of the drop trigger a nonlinear oscillation when the drop falls. The initial shape of the drop when it is just formed is decomposed into spherical harmonic modes. The initial mode amplitudes, characterized by the Fourier-Legendre coefficients, are found to be finite for up to the tenth mode. The pinching dynamics such as interface overturning introduces small-scale variation on the drop contour, which in turn contributes to the finite amplitudes of the higher-order modes. Furthermore, the initial kinetic energy when the droplet is just formed is as important as the initial surface energy contained in the drop shape, and is found to amplify the initial oscillation amplitude and to induce a phase shift in the oscillation of all the modes. By incorporating both the initial surface and kinetic energy, the linear model for a free drop oscillation yields very good predictions for the second and third modes. The mode amplitude spectra show both the primary frequencies that are consistent with the Lamb's theory and the secondary frequencies arising from different modes due to nonlinear intermode coupling. Moreover, it is worth to noting that the nonlinear effect is most profound for the fourth mode owing to its resonant coupling with the dominant second mode. The complex transient flow inside and outside the drop is induced by the interaction between the falling motion and the nonlinear oscillation. The streamlines indicate that the internal flow is substantially different from the Hill vortex for a falling drop without oscillation. The temporal evolutions of both the internal flow and the wake morphology follow the dominant second oscillation mode. In the oblate-to-prolate deformation, the internal flow goes against the external flow. As a result, a saddle point arises in the drop, which gives rise to two counterrotating vortices. The vortex dynamics are visualized by the swirling-strength vortex identification criterion and the vorticity. Whereas the potential

*stanley_ling@baylor.edu
†abwang@iam.ntu.edu.tw

flow changes direction during a second-mode oscillation cycle, the rotating directions of the vortices remain the same.

I. INTRODUCTION

The falling dynamics of an oscillating drop is essential to many natural phenomena and industrial applications, such as rain drops [1] and inkjet printing [2]. For drops that are formed by a nozzle, the drop characteristics can be controlled through the inflow rate. When the inflow rate is large, the injected liquid inertia dominates and the drop formation is in the jetting regime; when the inflow rate is small, then gravity plays the dominant role, placing the drop formation in the dripping regime [3]. In the present study, we focus on one specific case in the dripping regime. The purpose of the study here is to provide a comprehensive description of the short-term oscillation and falling dynamics for the dripping drop.

The initial conditions for the drop fall are determined by the drop formation process. Since the shape oscillation of the falling drop is triggered by the nonequilibrium shape and the velocity field when the drop is just formed. The shape oscillation will in turn impact the falling dynamics of the drop and the development of the transient flow around the drop. Nevertheless, despite its importance, the effect of drop formation on the subsequent oscillation and falling dynamics have not received enough attention in former studies. Instead of using the precise post-drop-formation state, *ad hoc* initial conditions (such as simple spheroid shape) are often used in simulations [4–6]. To fully incorporate the effect of drop formation, the whole process starting from drop growth, continuing with detachment, and eventually fall is considered in the present simulation. Another important advantage of simulating the whole process is that an experiment with exact conditions can be done to validate the simulation results. This is hard to achieve if *ad hoc* initial conditions are specified like in former simulations.

A. Drop formation

The dripping drop first develops as a pendant drop, hanging at the nozzle exit. When the drop volume is smaller than the critical volume, the surface tension is strong enough to resist gravity and to keep the drop stably attached to the nozzle [7,8]. As the volume of the pendant drop reaches the critical value, the drop becomes unstable and a neck is formed between the nozzle and the main body of the drop [9,10]. The minimum radius of the neck rapidly decreases, giving rise to an increasingly large capillary pressure in the neck. This high pressure drives the liquid away from the neck toward the nozzle and the main body of the drop, further accelerating the pinching process.

The pinching of the liquid neck will eventually detach the drop from the nozzle, and the pinching dynamics has been studied extensively in the past. The overall pinching process is dictated by surface tension, inertial, and viscous forces [11]. The pinching process exhibits a finite-time singularity and a universal self-similar behavior near the singularity [12–19]. For low-viscosity liquids like water, inertia of the liquid flow toward the main body of the drop results in the shift of the local minimum of bridge radius toward the top of the drop, where the interface overturns before pinching eventually occurs.

To obtain details of the flow field in the drop formation process, advanced experimental diagnostics and high-resolution simulations are required [20–22]. By recording two consecutive images of the same drop with a small time delay, van der Bos *et al.* [21] extracted the longitudinal velocity profile during drop formation. For the present problem, the viscosity and density of the surrounding air are small compared to those for water, and the effect of the surrounding air on drop formation is small. When the surrounding fluid has similar density or viscosity as the drop fluid, the surrounding fluid can have a significant impact on the drop formation dynamics [23].

B. Oscillation of a free drop

Following the formation, the drop falls under the action of gravity. Since the shape of the drop just after detachment is out of equilibrium, the capillary force will cause the drop to oscillate when it falls. Drop oscillation is a classic fluid mechanics problem, and the early investigation on the oscillation of a free drop can be traced back to the pioneering work of Rayleigh [24]. (A free drop here is referred to a drop that is located in an unbounded domain without gravity and falling motion.) For the infinitesimal amplitude oscillation of a free and inviscid liquid drop, Rayleigh decomposed the shape of the drop into spherical harmonic modes and calculated the corresponding frequency for each mode [24]. The original work of Rayleigh is based on a free-surface approximation. The extension to incorporate the effect of ambient fluid and the viscous effect was made by Lamb [25], and later followed by others [26–28]. Lamb's theory is generally valid for low-viscosity fluids. Yet Miller and Scriven [27] showed that even if the viscosities of the drop and surrounding fluid are both small, the viscous effect cannot be ignored since the oscillation damping rate is controlled by the boundary layer developed near the interface. The transient effect on the oscillation frequency and the damping rate was investigated by Prosperetti [28], and it is shown that the predictions based on normal mode analysis by Lamb [25] are strictly valid only asymptotically. When the oscillation amplitude is finite, the nonlinear effect on drop oscillation becomes important. Typical nonlinear effects include decrease of oscillation frequency with oscillation amplitude, asymmetry in oscillation amplitude, and coupling between different oscillation modes [29–33].

C. Dynamics of a falling drop

For a falling drop, the oscillation dynamics and the transient flow around the drop become more complicated. Extensive numerical and experimental studies have been performed to understand the long-term falling dynamics of liquid drops after the terminal velocity is reached (see, for example, Feng and Beard [1], Gunn [34], Helenbrook and Edwards [35], Feng [36]). Those research efforts were usually motivated by the interest in rain drops in atmospheric science. The present study has a different focus, that is, on the short-term dynamics of the falling drop. Here the short term and long term are defined with respect to the response time required for the drop to reach the terminal velocity. The interest on the short-term behavior is motivated by the fact that, for many application of falling drops, such as inkjet printing, the drop will reach a substrate or a liquid film far before reaching the quasisteady state. Furthermore, the oscillation dynamics of a falling drop in the short term has also lead to new technology to measure liquid properties, e.g., Staat *et al.* [37] recently proposed new methods to measure surface tension and drop viscosity based on the short-term oscillation frequency and damping rate.

In the short term, the drop velocity and Reynolds number increase over time, and the viscous flow around the drop is transient. Furthermore, due to the falling motion and the induced shear stress, the equilibrium shape of the oscillating drop is not spherical in general [36]. Because of these additional complexities, there is no general analytical solution for the problem, and numerical approaches are required to solve the governing equations [4–6,38]. Owing to the similar dynamics between a falling drop and a rising bubble, these two cases are often discussed together (see, for example, Ern *et al.* [39]), although a fundamental difference between these two cases exists [38]. It is challenging to accurately measure the three-dimensional (3D) flow inside a small drop in experiments. By seeding tracer particles of an average size of 10 μm, Chung and Trinh [40] obtained instantaneous velocity maps inside an oscillating drop which is electrostatically levitated.

D. Numerical simulation

Thanks to the development of advanced interface capturing techniques in the past decades, direct numerical simulation is now capable of capturing interfacial flows that exhibit topology changes [41] and can also provide high-level details of the flow field that are difficult to measure

in experiments. Extensive numerical studies have been conducted to simulate the drop formation process by the volume-of-fluid (VOF) method; see, for example, Zhang [42] and Gueyffier *et al.* [43]. The recent simulations by Agrawal *et al.* [5] have used the VOF method to resolve the oscillation of a falling drop with a nonspherical initial shape. It is shown that the oscillation arises only in the longitudinal direction, and no azimuthal variation was observed even when vortex shedding occurs in the wake of the drop. Another recent work by Bergeles, Hardalupas, and Taylor [6] presented high-resolution 3D simulation results for a falling drop of millimeter class. The detailed flow structure was well captured, and in particular, the roller vortex that is required to link the circulation in the wake of the drop with a Hill vortex inside the drop was clearly unveiled. For a similar problem, Lalanne, Tanguy, and Risso [4] have performed axisymmetric simulations using the level-set method for the oscillation of rising drops and bubbles. It was found that the oscillation frequency decreases slightly with the rising velocity while the damping rate of the drop oscillation is significantly magnified due to the rising motion.

E. Goal of this study

In spite of of the extensive studies discussed above, a comprehensive understanding of the short-term oscillation and falling dynamics for a dripping drop remains to be established. In particular, the effect of drop formation on the oscillation dynamics and the transient flow around the falling drop are still not fully understood. To the knowledge of the authors, there is no previous study that considers the effect of the drop formation on the oscillation dynamics of a falling drop. The oscillation of a drop is dictated by the initial conditions, which are in turn set by the drop formation process. Former numerical studies generally assumed the initial drop shape to be ellipsoidal or spherical with a constant initial velocity within the drop [4–6]. However, the shape of the drop when it is just formed is far more complex than an ellipsoid, and furthermore, the velocity field in the just-formed drop is highly nonuniform due to the pinching dynamics. The former simulations with simplified initial conditions are useful to understand the general physics of oscillation of a falling drop. Nevertheless, in order to precisely predict the shape and dynamics of the falling drop, which are critical to many applications of drops, e.g., the impact of a falling drop on a deep pool [44], the effect of drop formation on the subsequent drop oscillation and falling dynamics must be faithfully incorporated.

The goal of the present study is therefore to investigate the dynamics of a water drop dripping in quiescent air through simulation and experiment. Particular focus will be placed on the drop oscillation dynamics and the development of the transient flow around the drop. To achieve this goal, one specific case is considered in the present study. The flow rate at the nozzle inlet is chosen to be sufficiently small, so that the drop formation is in the dripping regime and the drop growth is quasistatic. Furthermore, we focus on only the short term of the drop fall, during which the drop shape and the flow remain axisymmetric. The key questions that the present study aims to address include the following:

(1) Are the "initial conditions" set by the drop formation process important to the drop oscillation and falling dynamics?

(2) How do the nonlinear dynamics and falling motion influence the drop oscillation dynamics, such as the oscillation frequency and damping rate?

(3) How do the drop oscillation and the falling motion contribute to the development of the transient flow around the drop? Is the flow structure within the drop similar to the classic Hill vortex?

To address these questions, axisymmetric simulations are carried out with the adaptive multiphase flow solver GERRIS. An experiment with the same conditions has also been conducted to validate the simulation results. The simulation and experimental approaches are described in Sec. II. The results for drop formation, shape oscillation, and transient flow around the drop will be presented and discussed in sequence in Secs. III, IV, and V, respectively. Finally, concluding remarks will be given in Sec. VI.

TABLE I. Physical parameters for the formation of a dripping drop.

ρ_l (kg/m^3)	ρ_g (kg/m^3)	μ_l (Pa s)	μ_g (Pa s)	σ (N m)	R_0 (m)	g (m/s^2)	Q (μl/min)
1000	1.2	0.85×10^{-3}	1.8×10^{-5}	0.0688	8×10^{-4}	9.81	32

II. METHODOLOGY

A. Key parameters

The process of drop formation is controlled by physical parameters listed in Table I, including the liquid and gas properties, the nozzle radius, the gravity acceleration, and the inlet flow rate. The mean inflow velocity, $u_0 = Q/\pi R_0^2 = 0.265$ mm/s can serve as an alternative for the inflow rate Q. The key dimensionless parameters can be derived and the values are given in Table II. Since the gas-to-liquid density and viscosity ratios, r and m, are both very small, the effect of the gas phase on drop formation is small. The Weber, Ohnesorge, and Bond numbers are measures of the relative importance of the fluid inertia, liquid viscosity, and gravity with respect to surface tension. For the small Q used in the present problem, the drop formation process is quasistatic and We $= 8.17 \times 10^{-7} \ll 1$. The effect of inflow inertia is thus negligible. The variation of We does not influence the drop formation [20], and the value of Q is immaterial to the results to be presented, as long as Q remains to be small. Due to the relatively low viscosity of water, Oh $= 0.00426$ is also very small, suggesting that the viscous effect is generally small in the drop formation process. Finally, the Bond number is the primary dimensionless parameter to determine the sizes of the detached primary and secondary drop.

After the drop detaches from the nozzle, the drop radius is measured to be $R_d = 1.86$ mm. The oscillation and falling dynamics of the drop can be fully determined by the Reynolds and Weber numbers based on the drop diameter ($D_d = 2R_d$), namely, $\text{Re}_d \equiv D_d u_d \rho_g / \mu_g$ and $\text{We}_d \equiv D_d u_d^2 \rho_g / \sigma$, along with the postformation state of the drop as the initial conditions. As the drop velocity, u_d, increases over time, Re_d and We_d rise accordingly. In the time range considered in the present study, the drop velocity increases from 0.07 m/s (just after detachment) to about 1.70 m/s. The corresponding range of drop Reynolds and Weber numbers are $25.9 \lesssim \text{Re}_d \lesssim 633$ and $2.62 \times 10^{-4} \lesssim \text{We}_d \lesssim 0.156$. For this range of Re_d, the flow was observed to remain approximately axisymmetric in the experiment. It was measured that the deviation of the drop centroid from the nozzle axis is smaller than 0.3% of the falling distance in the time range considered. Furthermore, as We_d is small, the surface tension will be sufficient to avoid an aerobreakup. According to the experiment of Gunn and Kinzer [45], the terminal velocity for this drop size is about 6.2 m/s. The Reynolds and Weber numbers corresponding to the terminal falling velocity will then be about $\text{Re}_{d,t=\infty} \approx 1600$ and $\text{We}_{d,t=\infty} \approx 2.4$. It is clear that the drop velocity in the present study remains far from the terminal state. The drop oscillation Ohnesorge number, $\text{Oh}_{\text{osc}} = \mu_l / (\rho_l \sigma R_d)^{1/2}$, is often used to characterize the viscous effect on the oscillation of a free drop, which can be expressed as $\text{Oh}_{\text{osc}} = \sqrt{2\text{We}_d}/(m\text{Re}_d)$. (Alternatively, the oscillation Reynolds number, $\text{Re}_{\text{osc}} = 1/\text{Oh}_{\text{osc}}$, can be used.) Here $\text{Oh}_{\text{osc}} = 0.00278$, is very small; therefore, it is expected the viscous effect on the drop oscillation is small.

TABLE II. Key dimensionless parameters for the drop formation.

r ρ_g/ρ_l	m μ_g/μ_l	We $\rho_l u_0^2 R_0/\sigma$	Oh $\mu_l/\sqrt{\rho_l \sigma R_0}$	Bo $\rho_l g R_0^2/\sigma$
0.0012	0.021	8.17×10^{-7}	0.00426	0.091

Due to the rich flow physics involved in the present problem, we have focused on only one specific case instead of a parametric study. If the key dimensionless parameters listed in Table II vary, the specific values in the results to be shown later will change. However, the case selected here well represents millimeter-size low-viscosity droplets in the dripping regime. The conclusions with regard to the droplet formation, oscillation, and falling dynamics will remain valid as long as both of the Ohnesorge and Bond numbers are significantly smaller than unity. Parametric study for wider ranges of Oh and Bo is of interest but will be relegated to future work.

B. Modeling and simulation

1. Governing equations

The one-fluid approach is employed to resolve the two-phase flow, where the phases corresponding to the water drop and the ambient air are treated as one fluid with material properties that change abruptly across the interface. The incompressible Navier-Stokes equations with surface tension can be written as

$$\rho(\partial_t \boldsymbol{u} + \boldsymbol{u} \cdot \nabla \boldsymbol{u}) = -\nabla p + \nabla \cdot (2\mu \boldsymbol{D}) + \sigma \kappa \delta_s \boldsymbol{n}, \tag{1}$$

$$\nabla \cdot \boldsymbol{u} = 0, \tag{2}$$

where ρ, μ, $\boldsymbol{u}$, and p represent density and viscosity, velocity and pressure, respectively. The strain-rate tensor is denoted by $\boldsymbol{D}$ with components $D_{ij} = (\partial_i u_j + \partial_j u_i)/2$. The third term on the right-hand side of Eq. (1) is a singular term, with a Dirac distribution function δ_s localized on the interface, and it represents the surface tension. The surface tension coefficient is σ, and κ and $\boldsymbol{n}$ are the local curvature and unit normal of the interface.

The liquid volume fraction C is introduced to distinguish the different phases, in particular $C = 0$ in the computational cells with only air (respectively, $C = 1$ in cells containing only water), and its time evolution satisfies the advection equation

$$\partial_t C + \boldsymbol{u} \cdot \nabla C = 0. \tag{3}$$

The fluid density and viscosity are then determined by

$$\rho = C\rho_l + (1 - C)\rho_g, \tag{4}$$

$$\mu = C\mu_l + (1 - C)\mu_g, \tag{5}$$

where the subscripts g and l represent the gas phase (air) and the liquid phase (water), respectively.

2. Numerical methods

The Navier-Stokes equations [Eqs. (1) and (2)] are solved by the open-source solver GERRIS [46,47]. In GERRIS, a finite-volume approach based on a projection method is employed. A staggered-in-time discretization of the volume-fraction or density and pressure leads to a formally second-order accurate time discretization. The interface between the different fluids is tracked by solving the advection equation [Eq. (3)] using a VOF method [48]. A quadtree spatial discretization is used, which gives a very important flexibility allowing dynamic grid refinement into user-defined regions. Finally the height-function method is used to calculate the local interface curvature, and a balanced-force surface tension discretization is used [47,49].

3. Simulation setup

In the numerical model, the flow is assumed to be axisymmetric. The two-dimensional computational domain is shown in Fig. 1. The gravitational acceleration is along the z direction. The water is injected into the domain from the left, and the inlet flow rate Q is kept the same as in the
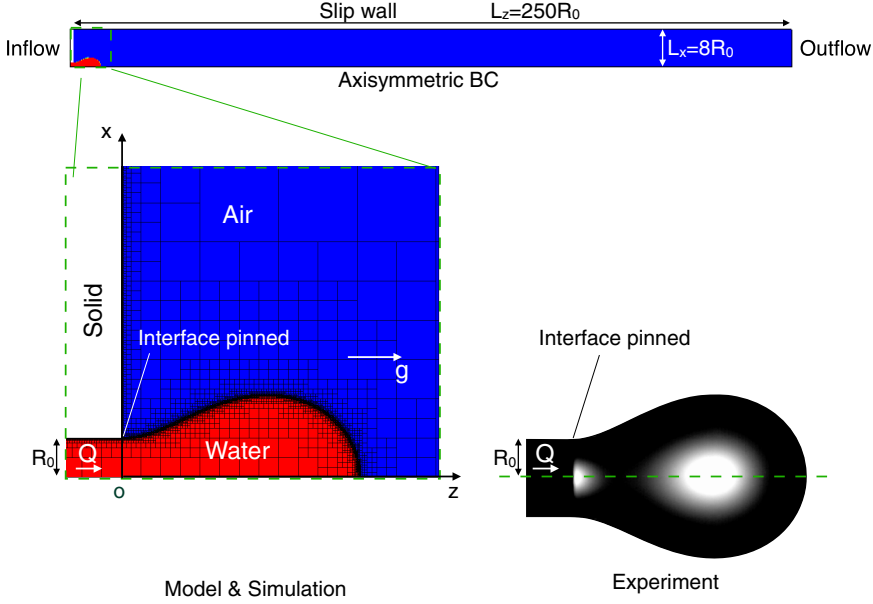
FIG. 1. Simulation setup.

experiment. The thickness of the nozzle wall is ignored in the model. The ratio between the inner and outer radii of the nozzle in the experiment is 0.75. It has been shown by Ambravaneswaran, Wilkes, and Basaran [50] that the nozzle wall thickness can affect the drop formation dynamics when the flow rate is high. For the present problem, a very small flow rate has been used. According to the experimental results of Zhang and Basaran [51] for similar small flow rates, the effect of the wall thickness becomes negligible if the ratio of the inner to the outer radii of the nozzle exceeds 0.2. The ratio in the present experiment is significantly larger than the critical value, and thus the effect of nozzle wall thickness on the drop formation can be ignored.

Furthermore, a solid block is added above the nozzle; see Fig. 1. The boundary condition of the volume fraction C at the solid boundary is $\partial C / \partial n = 0$. The reason for adding the solid block is to pin the contact line, where water, air, and solid meet, at the block corner. In the experiment, the interface is pinned at the outer perimeter of the nozzle. By setting the distance between this pinned point to the z axis as R_0, the model and the experiment exhibit the same Bo. In both experiment and simulation, the contact angle varies slightly when pinching occurs, and the contact line remains pinned during the drop formation process.

Thanks to the adaptive mesh, a computational domain that is significantly larger than the drop size can be used. As a result, the effect of boundaries on the drop can be eliminated. The length of the domain is $L_z = 200$ mm $= 250R_0$ and the height is $L_x = 6.4$ mm $= 8R_0$. The axisymmetric boundary condition is invoked at the bottom of the domain. The inflow (Dirichlet velocity and Neumann pressure conditions) and outflow (Dirichlet pressure and Neumann velocity conditions) BC's are applied to the left and the right of the domain. The top boundary is considered as a slip wall. The minimum cell size used in the simulation is determined by the maximum mesh refinement level, L, namely, $\Delta_{\min} = L_x / 2^L$. Different refinement levels have been tested, and the grid-refinement results are to be shown in the next section. The time step is computed based on the restriction from the advection, viscous, and surface tension terms in the governing equations. For the present problem, the time step restriction is mainly from the surface tension due to the small capillary number [52].
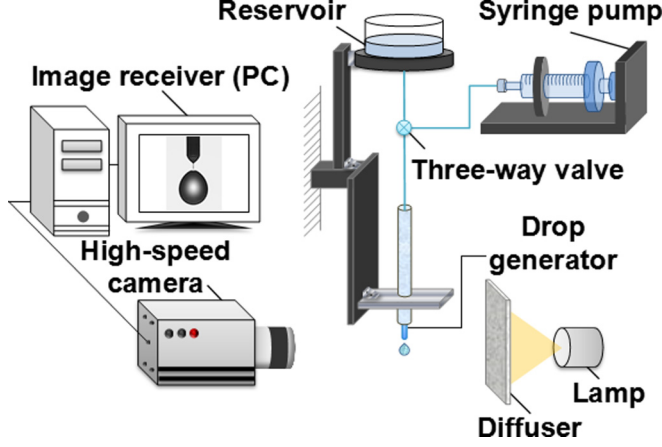
FIG. 2. Experimental setup.

C. Experiment

Figure 2 shows the experimental setup to investigate the formation and the fall of the water drop using high-speed imaging. A stainless steel nozzle with sharp-edged exit surface was used, and its inner and outer radii are 0.6 mm and 0.8 mm, respectively. Water drops were then generated from the nozzle either by the pressure from a constant-height reservoir or by the pressure from a syringe pump (KDS210, KD Scientific). A high-speed camera (NAC Memrecam GX-1) with frame rates varying from 100 to 5000 fps (frame per second) have been used to capture the shape of the drop. The spatial resolution and exposure time vary in the range 20–70 μm/pixel and 20–200 μs, respectively. To minimize the influence of vibrational disturbances and temperature variations in the pinching of the drop, all experiments were conducted on an antivibration table in the isolated corner of a basement with air conditioning. For better visualization, uniform illumination was achieved by placing a diffuser in front of the 100 W white light LED lamp. To avoid the heating effect, the LED light was placed 1.5 m away from the observation area, and the LED light was turned on only during recording. The images obtained by high-speed camera were postprocessed by Matlab code to measure the geometric properties of the drop before and after detachment, such as the volume and height of the pendant drop, the radius of the neck, the eccentricity of the falling drop.

Surface tension was measured with the Du Noüy ring method. Temperature (25 °C) and density of the test liquid were measured with a temperature recording device (Chino AH3760 with Pt100 sensor) and a mass-volume method, respectively. Liquid viscosity was determined using a rotational viscometer (Brookfield DV-II).

III. RESULTS FOR DROP FORMATION

The focus of the present study is on the oscillation and falling dynamics after the drop is detached from the nozzle. Nevertheless, since we aim at unveiling the effect of drop formation on the subsequent shape oscillation, the results for the drop formation will be first presented and validated against theory and experiment.

A. General process and timescales

A sequence of images of the drop obtained from high-speed imaging are shown in Fig. 3 to depict the process of drop formation and subsequent fall in quiescent air. The overall process can be generally divided into three phases: growth, pinch-off, and fall. When the drop falls, it deforms in an oscillatory manner.
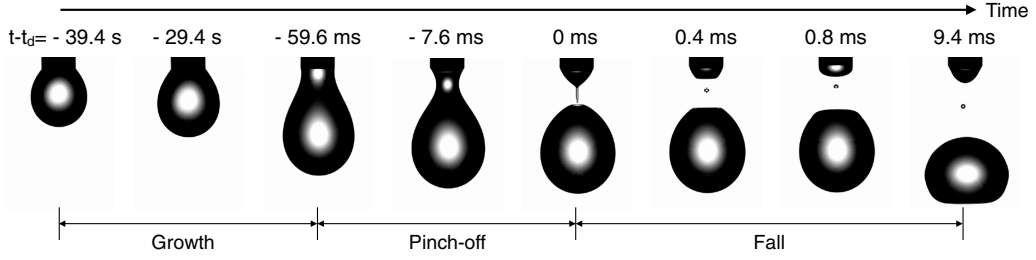
FIG. 3. Overall process of a drop dripping from a nozzle: growth, pinch-off, and fall shown by high-speed camera images.

It should be noted that the timescales for different phases in the process are different. (The time differences between the images shown in Fig. 3 are not even.) The growth of the drop is very slow compared to the other two phases, simply due to small flow rate at the nozzle inlet. It takes about 1 min for the pendant drop to grow to the critical volume. In contrast, when the drop volume reaches the critical volume, the developing and pinching of the neck of the pendant drop evolve at a very fast speed, taking about a millisecond. When the detached drop falls in air, the dominant oscillation period is about $\tau_{osc} = 21.5$ ms. This multiple timescale nature makes the investigation challenging for both experiment and simulation if one aims at capturing the whole process from drop formation to fall.

To overcome this challenge, multiple experiments with different frame rates were conducted to capture different phases. For the growth of the drop, a low frame rate, 100 fps, was used. For the pinching and oscillation, a high frame rate, 5000 fps, was used. The theoretical solution of a static pendant drop that is close to the critical volume is used to initialize the simulation. The initial velocity throughout the domain is taken to be zero since the pendant drop is quasistatic. For the most refined simulation ($L = 11$), the simulation starts at the time, that is, 394 ms, before the drop detaches, namely, $t_d - t = 394$ ms.

B. Drop growth as a pendant drop

Due to the small Weber and Ohnesorge numbers in the present problem, the effects of liquid inertia and viscosity on the drop formation are negligible compared to that of the surface tension. As a consequence, the drop grows quasistatically and follows the static pendant drop theory [7]. For a static pendant drop, its shape is axisymmetric, and the surface tension and the gravitational force are in equilibrium. The shape of the drop can then be obtained by solving a set of ordinary differential equations, which are given in Appendix A. The integration of the equations is from the bottom of the pendant drop as shown in Fig. 4 [a new coordinate (x', z') is used] with the curvature at the drop bottom κ_b as the boundary condition. For each κ_b, there are multiple solutions that satisfy
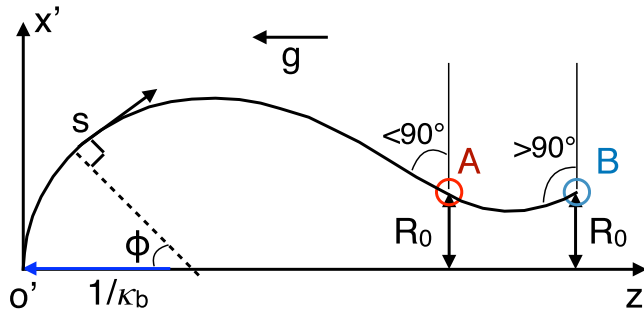

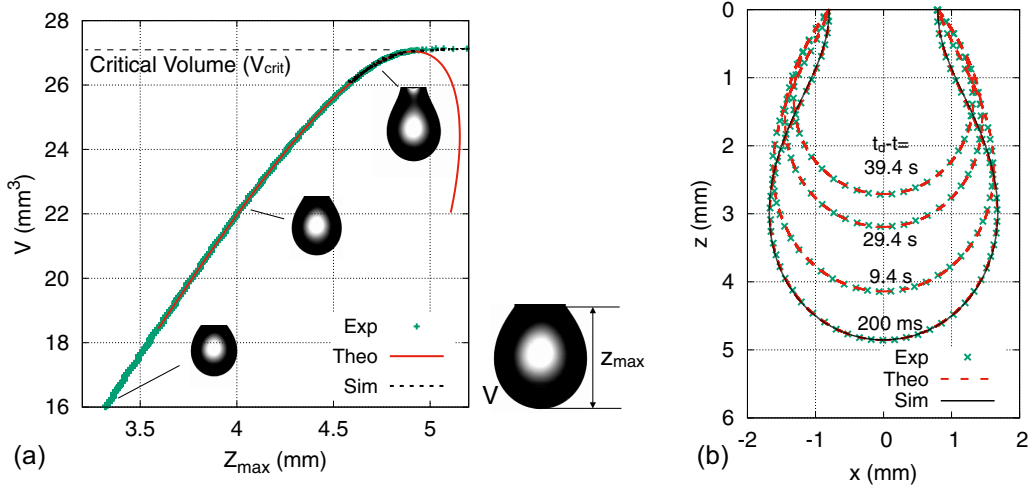FIG. 4. Sketch of the axisymmetric quasistatic pendant drop profile.

FIG. 5. Comparison of static pendant drop theory with experimental and simulation results: (a) drop volume V versus drop height Z_{max}; (b) drop contours at different times. The critical volume shown in (a) is $V_{crit} = 27.05$ mm³.

a given Bond number [10]. Here only the two solutions which give drop volumes which are close to the critical volume are relevant. The two solutions are schematically shown in Fig. 4. While for solution A the angle between the interface and the nozzle exit is less than 90°, for solution B the angle is larger than 90°.

The volume (V) and the height (Z_{max}) of the pendant drop can be measured from the experimental and numerical results, which are shown along with the pendant-drop theoretical predictions in Fig. 5(a). It can be observed the experimental and theoretical results agree very well before the drop volume reaches the critical volume. The critical volumes measured from the experiment and simulation are both about 27.10 mm³, which is very close to the value predicted by the pendant-drop theory, i.e., $V_{crit} = 27.05$ mm³. The V-Z_{max} curves obtained in the experiment and simulation appear to be flat when pinching occurs. During the pinching process, the rapid increase of Z_{max} is due to the redistribution of volume within the drop; as a result, the drop volume increase in the fast pinching process is negligibly small. The initial conditions for the simulation are taken from the theoretical result for $V = 26$ mm³. At the time, the angle between the interface and the nozzle exit is less than 90° (case A in Fig. 4). If the inflow at the nozzle is stopped, the pendant drop will remain stable. The simulation results of the V-Z_{max} curve at later times match very well with both the experiment and theory; see Fig. 5(a). This validates the present simulation setup in capturing the drop growth. The experimental and numerical results deviate from the theoretical solution beyond the critical z_{max}, since the latter represents an unstable static solution which will not be observed in reality.

The excellent agreement between the experimental and theoretical results is also achieved in the contours of the drop at different times, as shown in Fig. 5(b). The experimental results are shown to match very well with the theoretical predictions at 39.4, 29.4 and 9.4 s before pinching occurs. The simulation is started at $t_d - t = 394$ ms ($V = 26$ mm³). The simulation result at $t_d - t = 200$ ms (after the simulation has been run for a physical time of 194 ms) is compared to the theoretical and experimental results. The theoretical, numerical, and experiment curves all collapse perfectly, which again validates the present experimental and simulation approaches.

C. Pinching and drop detachment

As the pendant drop reaches the critical volume, it becomes unstable. The interface evolution during the pinching process for both simulation and experiment is shown in Fig. 6. The numerical
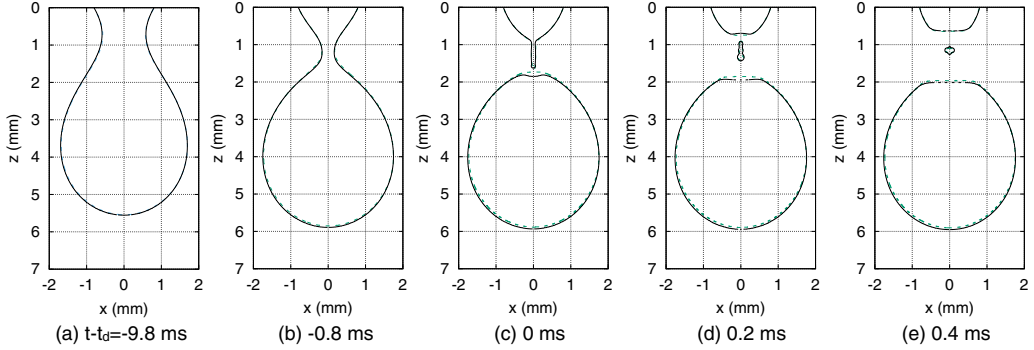
FIG. 6. Comparison between the numerical (solid lines) and experimental (dashed lines) results for the process of drop detachment.

and experimental results generally agree very well for the formation of the neck and the liquid bridge, the detachment of the primary drop, and the formation of the secondary drop. In Figs. 6(c)–6(d), there exists a small discrepancy in the drop contours between experiment and simulation. This is due to the concave shape at the top of the drop, which cannot be seen from the experimental images taken from the lateral side.

To better elucidate the pinching dynamics and the formations of the primary and secondary drops, temporal evolutions of the pressure and velocity fields are plotted in Fig. 7. As the drop reaches the critical volume, a "neck" develops between the nozzle and the pendant drop. The minimum radius of the neck (x_{min}) decreases rapidly over time. As a consequence, the pressure in the neck, which is inversely proportional to the neck radius, also increases rapidly. The pressure difference between the neck and the regions above and below the neck expels the liquid away from the neck with increasing velocity; see Figs. 7(a)–7(d). The thinning process of the neck contributes to the elongation of the pendant drop, and the neck turns into a thin liquid bridge. The minimum radius is initially located at about the center of the liquid bridge. The stagnation point is slightly higher than the location for the minimum neck radius. As the liquid accelerates from the stagnation point toward the attached liquid and the primary drop [see, e.g., Fig. 7(c)], the radius near the top and bottom of the bridge decreases faster than that near the center. The local radius minimum then shifts from the center to the bottom of the liquid bridge; see Fig. 7(d). Pinching first occurs at the location for the new minimum radius near the bottom of the bridge, detaching the primary drop. After the pinch-off, the liquid filament rapidly retracts upward from the pinch-off location. Due to similar effect of the inertia of the upward fluid motion, a new local minimum of radius develops at the top of the liquid bridge [see Fig. 7(g)], where soon another pinching happens. At the end, the liquid bridge is separated from the attached liquid and the primary drop, forming the secondary drop [see Fig. 7(h)]. A closeup of the secondary drop is also provided to show the high-resolution mesh used to resolve the pinching process. The dynamics of drop formation shown in the present experiment and simulation are consistent with former studies of drop formation [20,47,51] and filament breakup [11].

Since for the present problem Oh ≪ 1, the pinching process is mainly in the inertial regime where the temporal evolution of the minimum radius follows the 2/3 power law: $x_{min} \sim (t_d - t)^{2/3}$. As the new minimum radius shifts from near the center toward the two ends of the liquid bridge, the downward flow from the neck to the primary drop slows down, reducing the local Reynolds number and bringing the pinching dynamics into the viscous regime [11], where $x_{min} \sim (t_d - t)$. The temporal evolution of x_{min} for both experiment and simulation is plotted in Fig. 8(a), where the two power-law scalings and the transition from the inertial to viscous regimes can be clearly identified. As the viscous regime cannot sustain to the eventual breakup, another transition from the viscous regime to the inertial-viscous regime will occur in the pinching process at an even smaller timescale. Nevertheless, that timescale for the present problem with such a small Oh is hard to
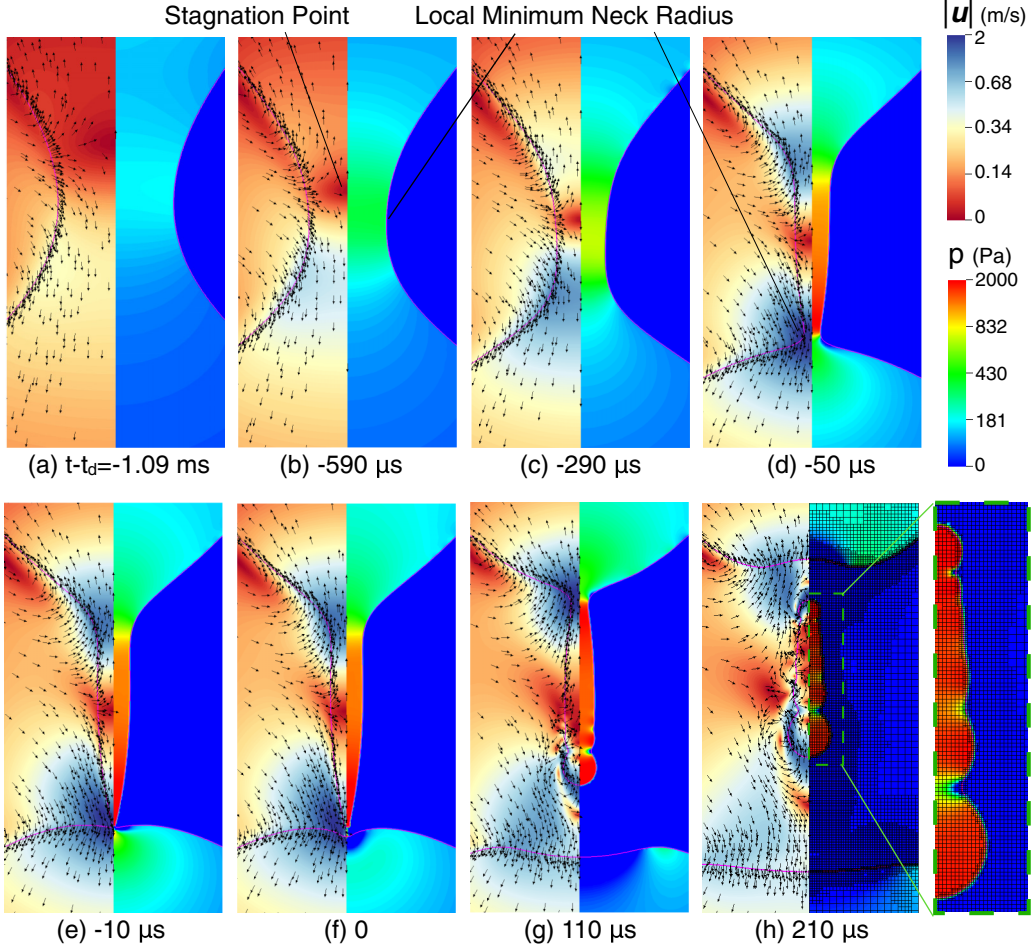
FIG. 7. Evolution of the velocity (left) and pressure (right) fields for the formation of primary and secondary drops. Skewed color scales have been used for better visualization.

resolve by simulation. Yet ignoring the inertial-viscous regime seems to introduce little effect on the formation of the primary drop.

The elongation of the drop due to the pinching process is measured and shown in Fig. 8(b). Again the numerical and experimental results agree very well. When the primary drop detaches from the liquid bridge, the drop height is about $z_{max}/R_0 = 7.35$. Similar experiments of dripping water drops by Zhang and Basaran [51] showed that $z_{max}/R_0 = 9.92$ and 5.58 for nozzle radius $R_0 = 0.4$ and 1.6 mm, respectively. In the present study, $R_0 = 0.8$ mm, so the drop height at the detachment time is in a good agreement with the experimental results.

Due to the low liquid viscosity in the present problem, when the liquid rushes from the neck toward the to-be-formed drop, the interface overturns before pinch-off occurs [15,17]. The overturning of the interface at the bottom of the liquid bridge can be identified with a careful look at Fig. 7(e). A closeup of the interface near the pinch-off location is presented in Fig. 8(c) to better show the overturning interface. The simulation results are shown to approach the self-similar solution given by Day, Hinch, and Lister [15]. For the same minimum radius $x_{min}/R_0 = 0.0028$, the overturning interface obtained in the present simulation agrees well with the inviscid flow result [15].

The excellent agreement between the simulation, experiment, and theoretical results for both drop growth and detachment fully affirms that the drop formation is well captured, and
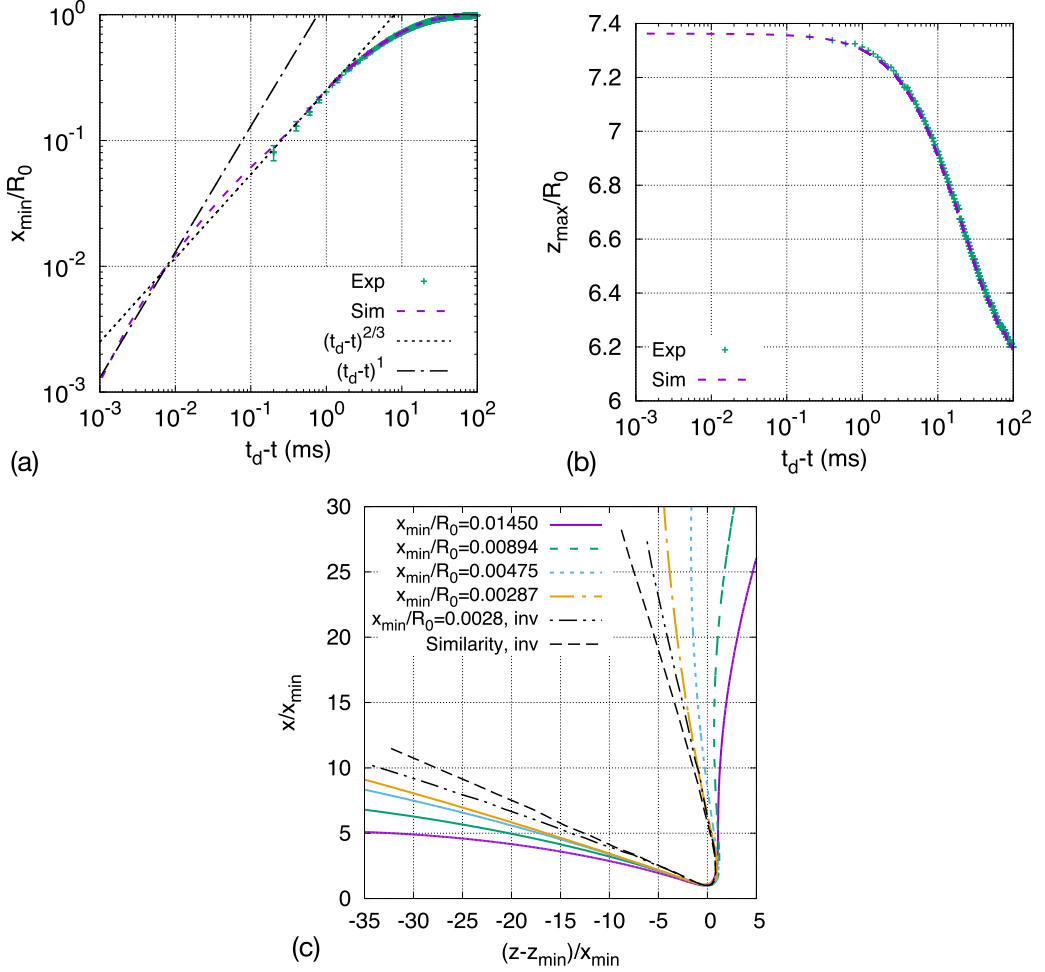
FIG. 8. Temporal evolution of (a) the minimum radius x_{min}, (b) the drop height z_{max}, and (c) the interface profiles near the pinching location prior to drop breakup. The dotted and dash-dotted lines in (a) indicate the $(t_d - t)^{2/3}$ and $(t_d - t)$ power laws for the inertial and viscous regimes, respectively. The error bars on the experimental data in (b) are smaller than the line thickness and thus are not plotted. The simulation results shown in (c) approach the inviscid self-similar solution provided by Day, Hinch, and Lister [15].

its effect on the subsequent fall of the drop has been faithfully incorporated in the present study.

IV. RESULTS FOR SHAPE OSCILLATION

A. Validation studies for oscillation and falling dynamics

When the drop is detached from the nozzle, the drop shape is elongated and out of equilibrium. Under the action of surface tension, the drop starts to deform and oscillate. The eccentricity of the drop, defined as the ratio between the height (b) and the width (a) of the drop, $e = b/a$, is a common parameter to characterize the shape deformation of an oscillating drop. The height b is defined as the difference between the minimum and maximum z coordinates of the droplet surface and thus does not account for the concave shape near the top of the drop shown in Fig. 6. The temporal evolutions of e obtained from simulations with different meshes are compared with the
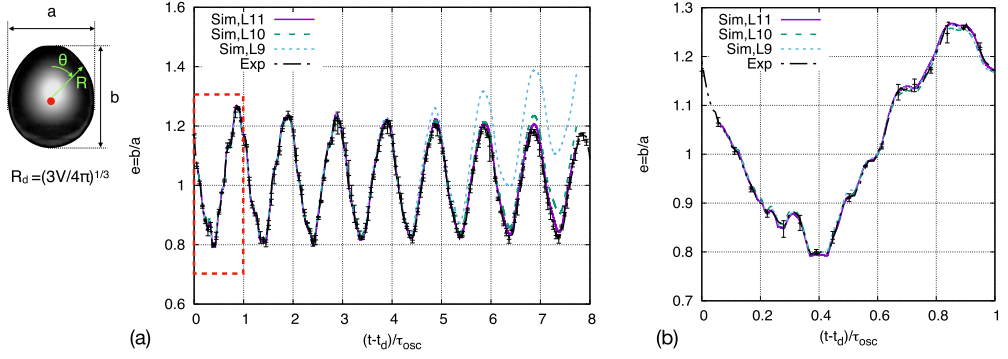
FIG. 9. Temporal evolution of the drop eccentricity for experiment and simulation. Here the eccentricity is defined as $e = b/a$, where b and a, as indicated, represent the height and width of the drop, respectively. The simulation results for different maximum mesh refinement levels (L) are compared to the experimental data in panel (a) and a closeup for $0 < (t - t_d)/\tau_{osc} < 1$ is given in panel (b). The corresponding minimum cell size Δ_{min} for $L = 11$, 10, and 9 are 3.12, 6.25, and 12.5 μm, respectively.

experimental measurement in Fig. 9. It is observed that the second mode dominates the oscillation of e, and the time period agrees well with that for the second mode of Lamb, $\tau_{2,Lamb}$. Therefore, $\tau_{2,Lamb}$ is taken to be the reference timescale for drop oscillation, namely, $\tau_{osc} = \tau_{2,Lamb}$, and in Fig. 9 time is normalized by τ_{osc}. This indicates that the falling drop retains similar dominant frequency (or periods) as for a free drop. This observation is consistent with the former studies [4,6,37].

The angular frequency for the nth spherical harmonic mode for small-amplitude oscillations of a free, viscous, and incompressible drop was derived by Lamb [25], which is given as

$$\omega_{n,Lamb}^2 = \frac{(n-1)n(n+1)(n+2)\sigma}{[(n+1)\rho_l + n\rho_f]R_d^3}. \tag{6}$$

The frequency is $f_{n,Lamb} = \omega_{n,Lamb}/(2\pi)$ (for convenience ω is simply referred to as "frequency" in the rest of the paper), and the time period is $\tau_{n,Lamb} = 1/f_{n,Lamb} = (2\pi)/\omega_{n,Lamb}$. For the second mode, the angular frequency is $\omega_{2,Lamb} = 292 \text{ s}^{-1}$, and the oscillation period $\tau_{2,Lamb} = 21.5$ ms. The Lamb frequencies for other modes, $\omega_{n,Lamb}$, for the present drop size are listed in Table III.

The simulation results for all the three mesh refinement levels agree well with the experimental data at early times as shown in Fig. 9(a), though the results for the coarser meshes deviate from the experimental data at later times. For example, the curve for $L = 9$ becomes different from the experimental data at about $(t - t_d)/\tau_{osc} > 4.6$. For the most refined case $L = 11$ ($\Delta_{min} \approx 3$ μm and $R_d/\Delta_{min} \approx 595$), the numerical and experimental results match remarkably well in the time range $[(t - t_d)/\tau_{osc} \lesssim 8]$ considered in the present study, indicating that $L = 11$ is necessary and adequate to resolve the present problem.

A closeup of the eccentricity evolution for $0 < (t - t_d)/\tau_{osc} < 1$ is presented in Fig. 9(b), from which it can be observed that the simulation results agree with experiment not only for the large-scale variation set by the dominant second mode, but also for the small-scale variations induced by the high-order oscillation modes. The temporal evolution of the drop centroid position is shown in Fig. 10(a). The simulation and experiment results again match very well. Since the falling motion of the drop is coupled with the shape oscillation, the excellent agreement in high-level details between simulation and experiment for both eccentricity and drop trajectories fully validates the simulation results for both falling and oscillation dynamics of the drop. It also confirms that the axisymmetric approximation made in the present simulation is valid up to the time range considered.

The evolution of the drop velocity, plotted in dimensionless form as the drop Reynolds number, is shown in Fig. 10(b). A dashed line is given to indicate the evolution of Re when the drop falls with no aerodynamic drag, namely, it undergoes a constant acceleration. In the short term, it is clear

TABLE III. Results for the spherical harmonic mode analysis for the oscillation of the falling drop. The frequency $\omega_{n,\text{Lamb}}$ and damping rate $\beta_{n,\text{Lamb}}$ are calculated following the linear theory of Lamb [25]. The primary frequency $\omega_{n,\text{sim}}$ is measured through the frequency spectrum of the computed Fourier-Legendre coefficients A_n. The value of A_n at $t = t_d$ is denoted by $A_{n,0}$, while the amplitude (α_n) of the oscillation of A_n at $t = t_d$ is represented by $\alpha_{n,0}$. The initial phase of the oscillation of A_n is denoted by ϕ_n. The values of $A_{n,0}$, $\alpha_{n,0}$, and ϕ_n are obtained from simulation results for drop formation. Exponential functions are used to fit the peaks and valleys of the temporal evolution of A_n for $n = 2, 3$. The fitted initial oscillation amplitudes and damping rates for peaks and valleys are represented by $\alpha_{n,0,\text{peak}}$ and $\alpha_{n,0,\text{valley}}$, and $\beta_{n,0,\text{peak}}$ and $\beta_{n,0,\text{valley}}$, respectively.

					n				
	2	3	4	5	6	7	8	9	10
$\omega_{n,\text{Lamb}}$ (s^{-1})	292.3	566.1	877.0	1223	1601	2009	2446	2909	3397
$\omega_{n,\text{sim}}$ (s^{-1})	306.8	552.2	859.0	1227	1595	2024	2454	2883	3436
$\beta_{n,\text{Lamb}}$ (s^{-1})	1.44	4.05	7.80	12.7	18.8	26.0	34.4	43.9	54.6
$A_{n,0}$	0.10	0.037	0.022	0.012	0.0066	0.0031	0.0011	-0.00045	-0.0014
$\alpha_{n,0}$	0.144	0.0672	0.0393	0.0280	0.0210	0.0165	0.0135	0.0110	0.0092
ϕ_n/τ_2	0.12	0.08	0.06	0.04	0.031	0.024	0.020	0.017	0.015
$\beta_{n,\text{peak}}$ (s^{-1})	1.35	4.12	–	–	–	–	–	–	–
$\beta_{n,\text{valley}}$ (s^{-1})	1.67	3.45	–	–	–	–	–	–	–
$\alpha_{n,0,\text{peak}}$	0.148	0.0673	–	–	–	–	–	–	–
$\alpha_{n,0,\text{valley}}$	0.141	0.0652	–	–	–	–	–	–	–

that the aerodynamic drag is small compared to the gravity force. The Reynolds number increases almost linearly, though a small discrepancy can be identified for $(t - t_d)/\tau_{\text{osc}} > 5$. The oscillation Reynolds number is $\text{Re}_{\text{osc}} = 1/\text{Oh}_{\text{osc}} = 360$. Initially Re_d is smaller than Re_{osc} but later overtakes and becomes larger than Re_{osc}. At $(t - t_d)/\tau_{\text{osc}} = 7.9$, the drop Reynolds number, $\text{Re}_d = 633$, is about 75% larger than Re_{osc}. Nevertheless, it is observed that the dominant oscillation frequency for the falling drop is still well predicted by Lamb's linear theory for a free drop.

B. Spherical harmonic mode decomposition

To better understand the shape oscillation of the falling drop, the instantaneous shape of the drop is decomposed into spherical harmonic modes [4,32]. The temporal evolution and frequency spectra
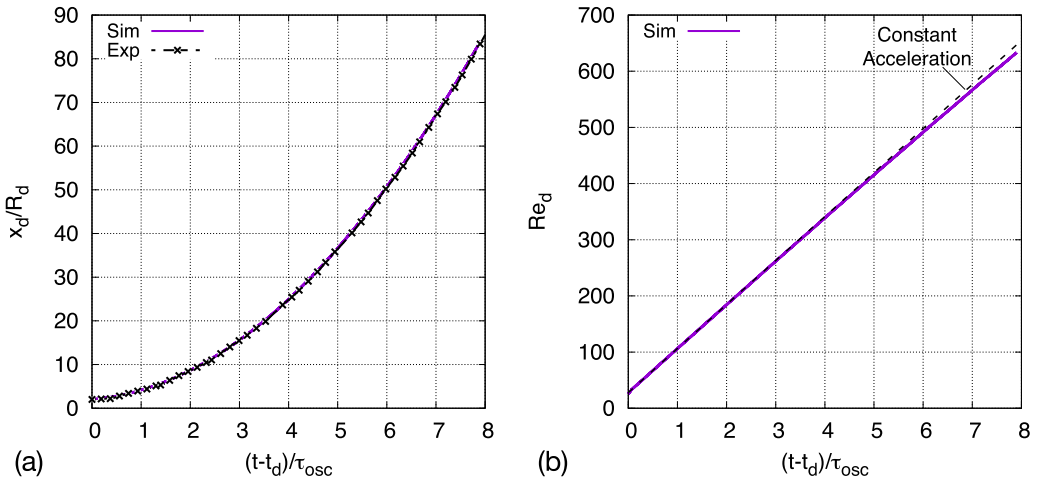

FIG. 10. Temporal evolutions of the drop centroid x position and Reynolds number Re_d.

of the mode amplitudes will be presented to analyze the effects of the drop formation, the nonlinear dynamics, and the falling motion on the shape oscillation.

The shape of an axisymmetric drop can be described by the radius of the drop contour with respect to the centroid R as a function of the colatitude θ (which is taken to be zero at the top of the drop), as shown in Fig. 9. For an oscillating drop, $R = R(\theta, t)$, and it can be expanded as the superposition of spherical harmonic modes as

$$\frac{R(\theta, t)}{R_d} = \sum_{n=0}^{\infty} A_n(t) P_n[\cos(\theta)], \tag{7}$$

where P_n is the Legendre polynomial of degree n and A_n is the corresponding Fourier-Legendre coefficient, which represents the amplitude of the nth spherical harmonic mode. Assuming incompressibility, the drop volume is fixed and $A_0 = 1$. Furthermore, for the analysis of the falling drop, a reference frame moving with the drop velocity is used, and the origin is set as the centroid of the drop. As a result, $A_1 = 0$. The temporal evolutions of A_2 to A_{10} for the simulation results are shown in Fig. 11. A grid refinement study has been performed to confirm that the results presented are mesh independent; see Appendix B.

The Fourier-Legendre coefficients at $t = t_d$ are denoted as $A_{n,0}$, and the values are listed in Table III. The initial amplitudes for spherical harmonic modes generally decrease with the mode number n. The amplitudes of higher order modes ($n > 2$) are finite and cannot be ignored. For example, $A_{5,0}$ and $A_{7,0}$ are about 11% and 3% of $A_{2,0}$, respectively. The small-scale spatial variations in the drop contours near the top of the drop [see Fig. 6(c)], which are in turn induced by the pinching process, contribute to the finite amplitudes of the high order oscillation modes.

The frequency spectra of A_n are shown in Fig. 12, from which the primary frequency for each mode can be identified. The values of the primary frequencies for simulation, $\omega_{n,\mathrm{sim}}$, are given in Table III. It can be seen that the oscillation frequency agrees well with the Lamb frequency. This conclusion is valid not only for the dominant $n = 2$ mode (as already shown in Fig. 9) but also for other modes up to $n = 10$. It can be observed from Fig. 11 that, at the end of the simulation, $(t - t_d)/t_{\mathrm{osc}} \approx 7.9$, the drop Reynolds number, $\mathrm{Re}_d = 633$, is about 75% larger than $\mathrm{Re}_{\mathrm{osc}}$, yet the agreement with the Lamb frequency is still very good.

According to the nonlinear analysis of Tsamopoulos and Brown [29], the leading term in the decrease of oscillation frequency due to finite amplitude is second order. For the dominant second mode, the initial amplitude $A_{2,0}$ is about 10%. The correction of frequency due to nonlinear effects is about 1%, which is quite small. This explains why the linear theory of Lamb [25] remains a very good approximation for present case, even though the mode amplitudes are finite.

C. Linear oscillation of a free viscous drop

The short-term oscillation of the drop is mainly controlled by the capillary effect; however, it is also significantly affected by the drop formation, the nonlinear dynamics due to finite oscillation amplitudes, and the falling motion. To better understand these effects on the oscillation dynamics, the simulation results are compared to the linear theory of Lamb [25] for the linear oscillation of a free viscous drop.

The Fourier-Legendre coefficients for the nth Lamb mode, $A_{n,\mathrm{Lamb}}$, are given as

$$A_{n,\mathrm{Lamb}}(t) = \alpha_n \cos[\omega_{n,\mathrm{Lamb}}(t + \phi_n)]. \tag{8}$$

For a viscous drop, the oscillation amplitude α_n decreases in time due to viscous dissipation. For small $\mathrm{Oh}_{\mathrm{osc}}$, the viscous damping effect causes an exponential decay of α_n,

$$\alpha_n(t) = \alpha_{n,0} \exp(-\beta_{n,\mathrm{Lamb}} t), \tag{9}$$
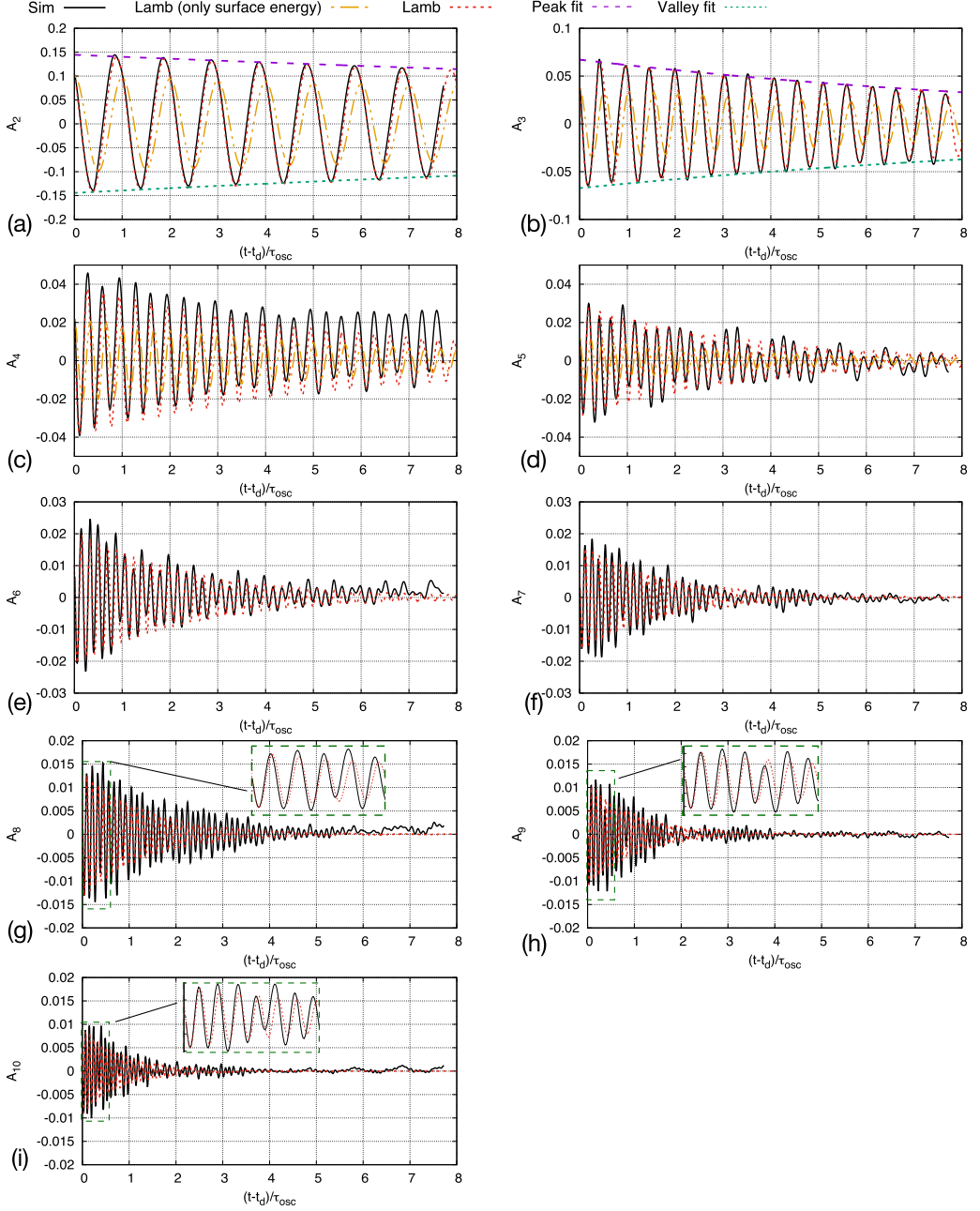
FIG. 11. Temporal evolutions of the Fourier-Legendre coefficients, A_n, for different spherical harmonic modes, comparing the simulation results with the linear free-drop model based on the theory of Lamb [25], with and without the initial kinetic energy. The exponential decay of the oscillation amplitudes for the peaks and valleys is also indicated in (a) and (b) for $n = 2$ and 3 modes.

where $\beta_{n,\mathrm{Lamb}}$ is the damping rate, given by Lamb [25] as

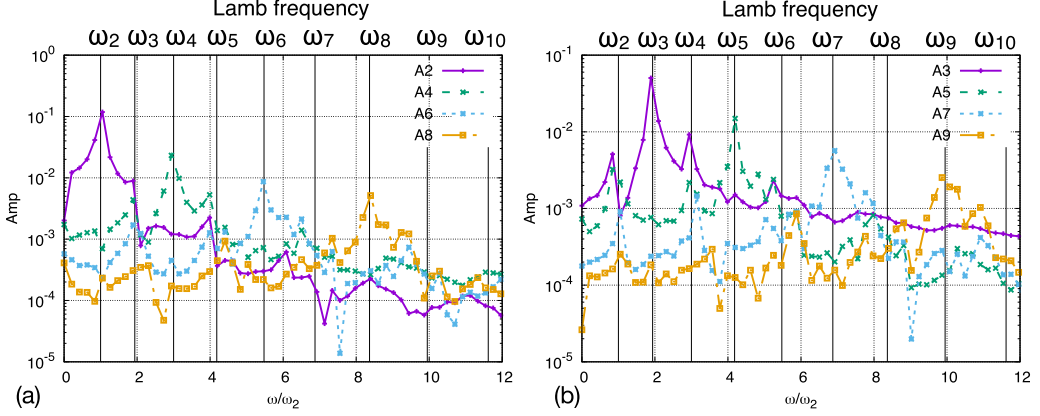$$\beta_{n,\mathrm{Lamb}} = \frac{(n-1)(2n+1)\nu_l}{R_d^2}. \tag{10}$$

FIG. 12. Frequency spectra of Fourier-Legendre coefficients for (a) even and (b) odd spherical harmonic modes, indicating the effect of mode coupling.

Then Eq. (8) can be rewritten as

$$A_{n,\mathrm{Lamb}}(t) = \alpha_{n,0} \exp(-\beta_{n,\mathrm{Lamb}}t) \cos[\omega_{n,\mathrm{Lamb}}(t + \phi_n)]. \tag{11}$$

The viscous damping influences the oscillation frequency as $\omega_n^{*2} = \omega_{n,\mathrm{Lamb}}^2 - \beta_{n,\mathrm{Lamb}}^2$. For the present problem $\beta_{n,\mathrm{Lamb}} \ll \omega_{n,\mathrm{Lamb}}$ (see Table III), and as a result, the decrease of frequency due to viscous effect is negligible. This also explains why the dominant oscillation frequency agrees so well with the Lamb frequency [Eq. (6)] as already shown in Fig. 9.

In Eq. (11) there are in total four parameters, $\omega_{n,\mathrm{Lamb}}$, $\beta_{n,\mathrm{Lamb}}$, $\alpha_{n,0}$, ϕ_n. The frequency $\omega_{n,\mathrm{Lamb}}$ and damping rate $\beta_{n,\mathrm{Lamb}}$, as shown in Eqs. (6) and (9), depend only on the fluid properties. In contrast, the initial oscillation amplitude of the Fourier-Legendre coefficient, $\alpha_{n,0}$, and is the initial phase, ϕ_n, are determined by the drop formation process and the resultant postformation state, including both the shape (surface energy) and the velocity field (kinetic energy).

D. Effect of the initial kinetic energy in the drop

Conventionally, the surface energy contained in the initial shape is assumed to dominate the initial state of drop oscillation, and the initial kinetic energy (velocity field) is usually ignored. The present study that covers both the drop formation and subsequent oscillation provides an opportunity to reexamine this assumption.

If the kinetic energy in the initial condition is ignored, i.e., the velocity field is zero everywhere, or a static drop with the same shape as the postformation drop is released, then $\alpha_{n,0} = A_{n,0}$ and $\phi_n = 0$, and Eq. (11) becomes

$$A_{n,\mathrm{Lamb,surf}}(t) = A_{n,0} \exp(-\beta_{n,\mathrm{Lamb}}t) \cos[\omega_{n,\mathrm{Lamb}}(t)]. \tag{12}$$

The results of Eq. (12) for the first four modes ($n = 2$ to 5) are plotted in Fig. 11. It is clear that the model including only the surface energy in the initial state yields results that are very different from the simulation results, even though the Fourier-Legendre coefficients for the exact initial shape of the drop, $A_{n,0}$, have been used. A close examination of Fig. 11(a) indicates that the deviation starts right at $t - t_d = 0$. The computed A_2 decreases faster and to a lower minimum than that predicted by the model. The decrease of A_2 represents that the drop deforms from the prolate (elongated) to the oblate (flattened) shapes. Therefore, the drop in simulation is flattened faster and to a larger extent compared to the model prediction. The discrepancy is due to the remaining effect of pinching dynamics and the nonuniformly distributed kinetic energy in the postformation drop. As discussed above in Sec. III C, the high pressure in the liquid bridge expels fluid toward the drop (which even

induces overturning of the interface at the top of drop). As a consequence, when the drop is just detached from the liquid bridge, the top portion of the drop retains a significant downward velocity, which contribute to strengthening the prolate-to-oblate deformation, in addition to the capillary effect. The results clearly lead to the conclusion that the initial kinetic energy is as important as the initial surface energy to the shape oscillation and should not be ignored.

The key contributions of the initial kinetic energy to the shape oscillation are the amplification of $\alpha_{n,0}$ and the nonzero initial phase angle ϕ_n. The values of $\alpha_{n,0}$ and ϕ_n for different modes can be obtained by fitting Eq. (11) with the simulation results near $t - t_d = 0$. As shown in Table III, $\alpha_{n,0} > |A_{n,0}|$ and $\phi_n \neq 0$ are true for all the modes considered here. The amplification of $\alpha_{n,0}$ and the nonzero initial phase angle due to drop formation were also observed in the experiments of Becker, Hiller, and Kowalewski [31], though the physics behind them was not discussed. With the corrected $\alpha_{n,0}$ and ϕ_n, Eq. (11) yields a much better agreement with the simulation results for the whole time range considered; see Fig. 11. [Hereafter, Eq. (11) with corrected values of $\alpha_{n,0}$ and ϕ_n is referred to as the linear free-drop model.] Considering the fact that the linear free-drop model still ignores the effects of falling motion and nonlinear dynamics, the agreement between the model and the simulation is quite impressive for the $n = 2$ and 3 modes.

In spite of the apparent good agreement between the linear free-drop model and the simulation results for the lower-order modes ($n = 2, 3$), significant differences exist in the higher-order modes ($n \geqslant 4$). At early time ($t \lesssim 5\tau_{\text{osc}}$) the falling velocity is small and thus the effect of the falling motion is negligible; the discrepancy is thus mainly due to the nonlinear effects, which are in turn triggered by the finite mode-amplitudes when the drop is formed. At later time, when the drop velocity becomes large, $\text{Re}_d > \text{Re}_{\text{osc}}$, the contribution of the falling motion to the discrepancy becomes significant. These two effects are discussed in sequence in the following sections.

E. Effect of mode coupling and energy transfer

As summarized by Becker, Hiller, and Kowalewski [31], typical nonlinear effects in shape oscillation include (a) the dependence of the oscillation frequency on the amplitude, (b) the asymmetry of the oscillation amplitude, and (c) the coupling between modes. As shown in Fig. 9 the variation in frequency is small for the present case; however, the other two nonlinear effects can be clearly identified.

A close look at Fig. 11 shows that the oscillation amplitude of A_n is generally asymmetric, namely, the oscillation amplitudes corresponding to the peaks and valleys are different. The asymmetry of oscillation amplitude is most profound for the $n = 4$ mode: the temporal evolution of A_4 is clearly shifted upward; see Fig. 11(c). (A physical explanation for the strong nonlinear effect for the $n = 4$ mode is to be given later.) Similar but less obvious upward shifting in the mode amplitude evolution can also be identified for the $n = 6$ and 8 modes. The asymmetric behavior is less obvious for the lower-order modes ($n = 2$ and 3). To better illustrate the asymmetric behavior, the exponential function [Eq. (9)] is used to fit the peaks and valleys of the temporal evolutions of A_2 and A_3. The fitted initial amplitudes and damping rates for the peaks and valleys are different as shown in Table III. It is shown that $\alpha_{n,0,\text{peak}} > \alpha_{n,0,\text{valley}}$ for both $n = 2$ and 3 modes. For the damping rate, $\beta_{2,\text{peak}} < \beta_{2,\text{valley}}$ while $\beta_{3,\text{peak}} > \beta_{3,\text{valley}}$. The damping rate prediction of Lamb [Eq. (10)] lies between the damping rates for the peaks and valleys. Due to the strong nonmonotonicity in the decay of the oscillation amplitude for the higher-order modes, it is infeasible to fit the amplitude with an exponential function.

Another important nonlinear effect on drop oscillation is the interaction between different spherical harmonic modes through energy transfer. When energy is added or extracted from a specific mode, the oscillation amplitude of that mode will be amplified or suppressed, respectively. As a result, the decay of oscillation amplitude becomes nonmonotonic; see Figs. 11(d)–11(i). It is conventionally considered that the nonlinear effects arise due to a large amplitude; however, it is observed here that the nonlinear effect is stronger for the higher-order modes ($n \geqslant 4$) than the lower-order modes ($n = 2, 3$) while the amplitudes of the former are actually smaller than of

the latter. This interesting behavior has also been observed in experiments and can be explained through mode coupling [31]. For the present problem, the energy stored in the lower-order modes is significantly larger than that in the higher-order modes; see $\alpha_{n,0}$ values in Table III. Therefore, when there is a small energy transfer between the lower-order and higher-order modes, its effect on the lower-order mode amplitude is small, but it can modify the higher-order mode amplitude significantly.

Due to the large water-to-air density ratio in the present problem, the Lamb frequency is similar to the Rayleigh frequency

$$\omega_{n,\text{Rayleigh}}^2 = \frac{(n-1)n(n+2)\sigma}{\rho_l R_d^3}. \tag{13}$$

An important feature of the Rayleigh frequency is that ω_2 and ω_4 are commensurate ($\omega_4 = 3\omega_2$); see Table III. As a result, there exists a resonant effect in the coupling between the $n = 2$ and $n = 4$ modes [29,30]. As the $n = 2$ mode is the dominant mode that contains most of the oscillation energy, the $n = 4$ mode is modulated significantly due to the resonant energy transfer between the two modes. This explains why the nonlinear effect is always the most intense for the $n = 4$ mode.

The effect of mode coupling is also shown in the frequency spectra of the spherical harmonic mode amplitudes A_n; see Fig. 12. While the linear free-drop model yields a single frequency for each mode, $\omega_{n,\text{Lamb}}$ (indicated by the vertical lines), the spectra of computed A_n show multiple frequencies for modes $n > 2$. For the fundamental $n = 2$ mode, only the primary frequency ω_2 is observed. (Other smaller peaks in the A_2 spectrum correspond to the even number times of the primary frequency, such as $2\omega_2, 4\omega_2, 6\omega_2$.) For a given mode $n > 2$, the spectrum shows a primary frequency that agrees well with $\omega_{n,\text{Lamb}}$, and also multiple secondary frequencies corresponding to other modes (ω_m with $m \neq n$) which interact with the nth mode. In the spectrum of A_4, secondary frequencies $2\omega_2$ and $4\omega_2$ are observed (note the small difference between $4\omega_2$ and ω_5,) which is more evidence for its strong coupling with the $n = 2$ mode. A close look indicates that the A_6 spectrum also shows similar secondary frequencies at $2\omega_2$ and $4\omega_2$. Former studies have shown that an initial second-mode deformation will excite even modes due to mode coupling [29,32]. Therefore, though the coupling between the dominant $n = 2$ mode and other higher-order even modes like $n = 6$ is not as strong as with the $n = 4$ mode, their spectra also show the influence from the second mode.

Furthermore, a drop with initial finite-amplitude deformation of odd modes will transfer energy to the fundamental $n = 2$ mode and excite the oscillation of the latter [32]. In Fig. 12 a secondary frequency of ω_2 is observed in the spectra of the odd modes $n = 3, 5, 7, 9$. Due to the resonant coupling between the $n = 2$ and 4 modes, the oscillation energy from the odd modes can also be transferred to the $n = 4$ mode through the intermediary $n = 2$ mode. As a result, the spectra of the odd modes also show a secondary frequency ω_4. Finally, another commensurate relation exists between the $n = 5$ and 8 modes, namely, $\omega_8 = 2\omega_5$, and therefore, there exists a resonant coupling between the two. That explains why a secondary frequency ω_8 arises in the spectrum of A_5. It can be seen from Fig. 11 that, although the decay in oscillation amplitude is nonmonotonic due to mode-coupling, the viscous damping rates are generally consistent with Lamb's prediction (see the results for the linear free-drop model). However, the $n = 8$ mode seems to be an exception; the decay of oscillation amplitude is slower than the linear free-drop model, which is due to the resonant coupling between the $n = 5$ and 8 modes.

F. Effect of falling motion

The effect of the drop fall on the shape oscillation is initially small, yet as the drop falling velocity increases in time, its impact on drop oscillation is enhanced. The influence of the falling motion on the shape oscillation can be identified through the asymmetric oscillation amplitude. The asymmetric amplitude in A_n (such as $n = 4$) for $(t - t_d)/\tau_{\text{osc}} \lesssim 4$ is due to the nonlinear effect. If the drop does not fall, then as the oscillation amplitude decreases with time, the nonlinear effect
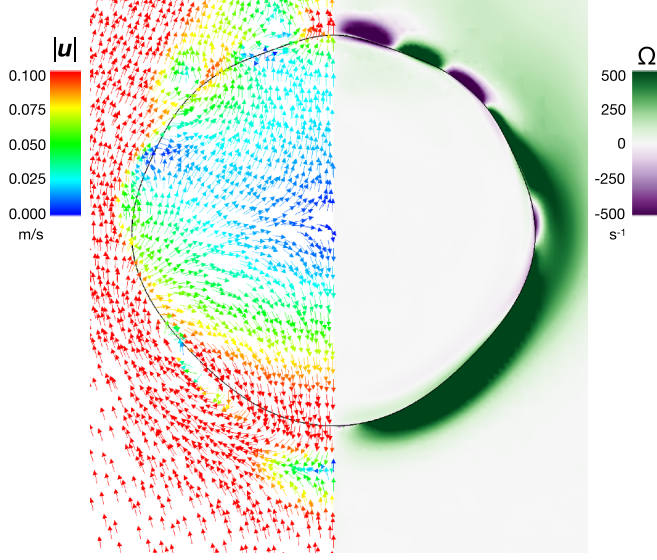
FIG. 13. Simulation results for the velocity (left) and vorticity (right) fields around the drop at $(t - t_d)/\tau_{\mathrm{osc}} = 0.56$.

will become weaker, and the level of asymmetry will also decrease over time. For the falling drop considered here, it is observed in Fig. 11(c) that the difference between the peak and valley amplitudes decreases initially but then remains at a similar level for $(t - t_d)/\tau_{\mathrm{osc}} \gtrsim 4$, which is due to the interaction between the drop and the external flow induced by the falling motion. In the long term when the drop reaches its terminal falling velocity (the drop can reach a fixed shape [36] or still oscillate [35] depending on $\mathrm{Re}_{d,\infty}$ and $\mathrm{We}_{d,\infty}$), the balance between surface tension and shear stress induced by the external flow results in a nonspherical equilibrium drop shape, which exhibits nonzero mode amplitudes ($A_{n,\mathrm{eq}} \neq 0$). Although the time period considered here is far from the equilibrium state, the shear stress induced by falling motion already has an impact on the drop shape and enhances the asymmetry in oscillation amplitudes. The asymmetric effect is reflected as an upward shit of A_n for the higher-order even modes ($n = 4, 6, 8, 10$) and is negligibly small for higher-order odd modes ($n = 5, 7, 9$). For the lower-order modes ($n = 2, 3$), the oscillation amplitudes are large, and thus the capillary effect dominates. Therefore, the effect of falling motion is less profound.

There also exists an energy transfer between the falling motion and the shape oscillation. It can be observed from Fig. 11(c) that for $(t - t_d)/\tau_{\mathrm{osc}} \gtrsim 4$, the oscillation amplitude decays much slower than the linear free-drop model. The energy dissipated by viscosity is compensated by the energy from the falling motion. Similar slower decay in oscillation amplitude for $(t - t_d)/\tau_{\mathrm{osc}} \gtrsim 4$ can also be observed in Figs. 11(d)–11(i) for other high-order modes.

V. RESULTS FOR THE TRANSIENT FLOW FIELD

The multimode oscillation of the falling drop is accompanied by a complex transient velocity field around the drop; see Fig. 13. The snapshot shown here is taken soon after the drop is formed, at $(t - t_d)/\tau_{\mathrm{osc}} = 0.5$, from the simulation results. The inward and outward motions of the interface can be observed from the velocity vector field. The oscillating motion of the interface induces swirling motion of the fluid near the drop, which can be visualized by the vorticity (Ω) field, as shown in the right half of Fig. 13.

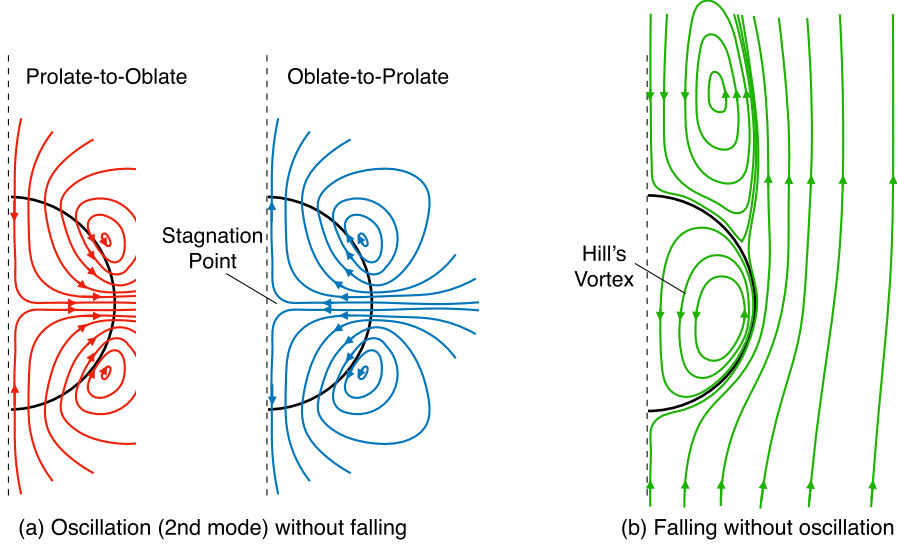(a) Oscillation (2nd mode) without falling   (b) Falling without oscillation

FIG. 14. Schematics of the flow field for (a) a drop that is oscillating without falling motion, and (b) a drop that is falling without oscillation. Panel (a) is adapted from our simulation of a free drop undergoing only second-mode oscillation. In panel (b) the streamlines are sketched based on the simulation results by Feng [36] for $Re_d = 200$ and $We_d = 1$.

A. Asymptotic limits

To better understand the development of the flow field for the falling and oscillating drop, we first look at the two asymptotic limits: (1) the case when the drop is freely oscillating but not falling, and (2) the case when the drop is falling but without oscillation.

A representative flow field around an freely oscillating drop is shown in Fig. 14(a). The simple case shown here contains only the second mode. As a response to the oscillation, two vortices are formed outside the drop with opposite rotation directions. The directions of the two vortices change within the oscillation cycle. When higher-order modes exist, more vortices will arise as can be seen in Fig. 13.

As the drop falls, it accelerates, and the relative velocity between the drop and the surrounding air increases in time until the terminal velocity is reached. When the drop Reynolds and Weber numbers are small, the drop will eventually reach a steady state. For this limiting case where the drop is falling without oscillation, the internal flow pattern is dictated by the external shear. In the Stokes limit, the drop shape will remain spherical, and the flow circulation inside the drop is known as the Hill vortex [53]. For finite but small Reynolds and Weber numbers, the drop will not be perfectly spherical, but the internal flow remains similar to Hill vortex [36]. A representative flow field for a falling drop without oscillation is shown in Fig. 14(b), which is sketched based on the simulation results of Feng [36] for $Re_d = 200$ and $We_d = 1$. There exists only one vortex, similar to the Hill vortex, inside the drop.

B. Flow patterns during one oscillation cycle

The interplay between the falling motion and the shape oscillation creates a complicated transient flow which is different from either of the two limiting cases. The evolution of the flow is illustrated with streamlines in the drop reference frame in Fig. 15. Since the second mode is dominant, the temporal variation of the flow pattern generally follows the cycle of the second-mode oscillation. The time range covered in Fig. 15 is $(t - t_d)/\tau_{osc} \approx 5$ to 6, namely, representing the sixth oscillation according to the second mode. The drop deforms from its prolate (elongated in the z direction)
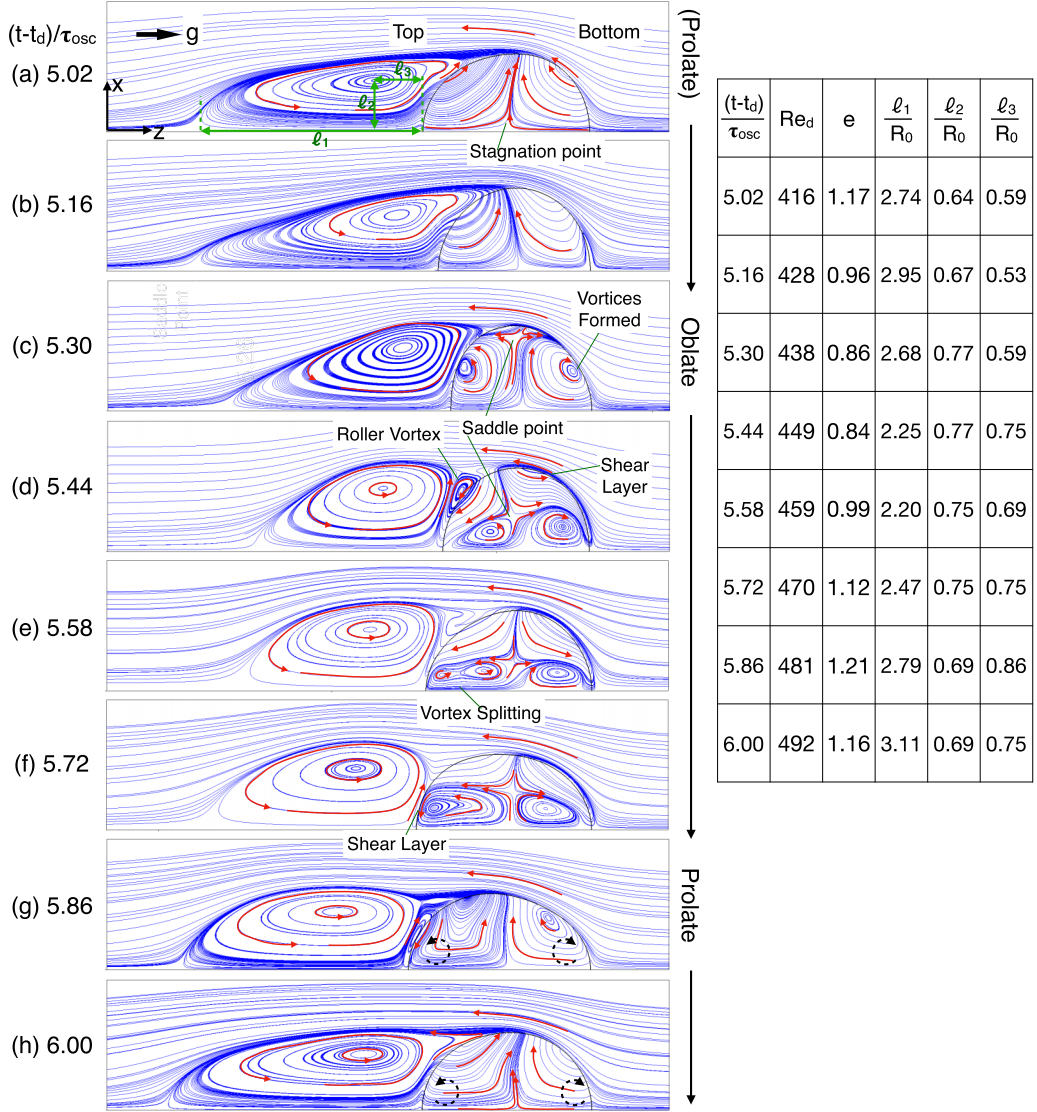
FIG. 15. Flow field near the oscillating and falling drop for $(t - t_d)/\tau_{osc}$ from 5 to 6. The characteristic length scales for the wake geometry, including the wake length l_1, the distance between the wake-vortex center and the axis l_2, and the distance between the wake-vortex center and the top of the drop l_3, are measured.

to oblate (flattened in z direction) shapes in Figs. 15(a)–15(c), reaching the most oblate shape at $(t - t_d)/\tau_{osc} \approx 5.30$. Then the drop returns back to the prolate shape from 15(c)–15(g), until a new cycle starts.

When the drop deforms from the prolate to the oblate shapes [see Figs. 15(a)–15(b)] the streamlines inside the drop are quite similar to those for the second-mode free oscillation. A stagnation point is formed when the fluid moves from the two poles toward the center. In the ground reference frame, the fluid velocity at that stagnation point is identical to the mean falling velocity of the drop. A close examination further shows that the stagnation point does not generally overlap with the centroid. In this time range, the external flow going over the drop is already strong enough to overcome the rotational flow induced by drop oscillations; therefore, the vortices outside the drop

that are seen in the free oscillation [see Fig. 14(a)] become invisible. At the colatitude θ about 45 and 135 degrees, the streamlines inside the drop align well with those outside. The internal flow corresponding to the prolate-to-oblate oscillation is enhanced by the external flow.

After the drop reaches the most oblate shape and starts to deform back [Figs. 15(c)–15(g)], the internal flow field becomes very different from that for the free oscillation shown in Fig. 14(a). For the freely oscillating drop, while the drop deforms from the oblate to the prolate shapes, the flow moves from the lateral side to the the stagnation point and then bifurcates toward the two poles [see Fig. 14(a)]. However, for the falling drop, as the original internal flow due to prolate-to-oblate oscillation is strengthened by the external flow, the oblate-to-prolate oscillation fails to reverse flow direction near the stagnation point. Indeed, the flow direction near the stagnation point does not change through the oscillation cycle. While the interface at the lateral side of the drop retracts toward the axis, the flow near the stagnation point still tries to move toward the lateral side. As a consequence, a saddle point (a saddle curve due to the axisymmetric geometry) is formed, which in turn induces two vortices (vortex tubes in the axisymmetric geometry) within the drop; see Fig. 15(c).

As the drop continues to deform towards the prolate shape, the saddle point is further pushed toward the z axis, so are the two vortices. Furthermore, as the internal circulations near the top and bottom of the drop are not aligned with the wake and the external flow [see Fig. 15(d)] roller vortices are formed outside the drop [6]. When the drop becomes more prolate, the two vortices inside are further flattened. At a certain point [see Fig. 15(e)] the internal vortex near the top of the drop splits into two.

After reaching the most prolate shape, the drop starts to deform back toward the oblate shape. In this process, as shown in Fig. 15(g), the two vortices inside the drop near the axis become invisible. However, they still exist, as will be shown later with vortex-identification techniques. It is just that the potential flow induced by the drop oscillation is so strong that the local swirling motion cannot be shown by streamlines. Two new transient vortices are formed inside the drop near the lateral side, which vanish very soon. Then the internal flow pattern returns to the form similar to the beginning of the cycle.

Within the time range considered the drop oscillation is still quite strong, e.g., the second-harmonic-mode amplitude remains larger than 0.1 as shown in Fig. 11. As a result, the fluid inertia due to oscillation plays a significant role in the transient flow inside the drop. It is important to note that the internal flow pattern observed here is substantially different from the Hill vortex, which corresponds to the long-term behavior when the drop oscillations are damped. In particular, the two vortices formed during the oblate-to-prolate process rotate in opposite directions compared to the corresponding external flows. Roller vortices are then formed between the internal and external flows to satisfy the fluid kinematics.

The formation of the saddle point during the oblate-to-prolate deformation is an important feature, which is due to the different directions of the flows induced by the external shear and the shape oscillation. Therefore, the Strouhal number, $\text{Sr} = u_{\text{osc}}/u_{ic}$, can be defined to characterize the formation of the saddle point, where u_{osc} and u_{ic} represent the characteristic velocities for the internal flows induced by the shape oscillation and by the external flow, respectively. While u_{osc} can be estimated as $u_{\text{osc}} \approx a_2\omega_2$, where $a_2 = A_2 R_d$ and ω_2 are the oscillation amplitude and frequency corresponding to the dominant second mode, u_{ic} can be approximated as $u_{ic} \approx u_d v_{ic}$, where v_{ic} is the internal circulation intensity [36]. The Strouhal number can be rewritten as $\text{Sr} = a_2\omega_2/(u_d v_{ic})$. When $\text{Sr} \to 0$, the droplet falls without oscillation [see Fig. 14(b)]. When $\text{Sr} \to \infty$ the drop oscillates without translational motion [see Fig. 14(a)]. For both these asymptotic limits, there is no saddle point in the flow. The saddle point will arise only when $\text{Sr} \sim O(1)$, namely, when u_{osc} and u_{ic} are comparable.

C. Wake topology evolution

The characteristic length scales for the wake geometry, including the wake length l_1, the distance between the wake-vortex center and the axis l_2, and the distance between the wake-vortex center and the top of the drop l_3, are measured over an oscillation cycle $(t - t_d)/\tau_{\text{osc}} = 5$ to 6 and are

shown in Fig. 15. The simulation results show that the wake length l_1 generally increases over time, which is consistent with former observations by Bergeles, Hardalupas, and Taylor [6]. At $(t - t_d)/\tau_{\text{osc}} = 5$ and 6, the drop eccentricity, e, is the same, while the wake length increases from $l_1/R_0 = 2.74$ to 3.11 due to increasing Re_d. The values here are larger than those obtained by Bergeles, Hardalupas, and Taylor [6] because of the larger Re_d. At $(t - t_d)/\tau_{\text{osc}} = 5$, $\text{Re}_d = 416$ and $l_1/R_0 = 2.74$, compared to $l_1/R_d = 2.2$ for the maximum $\text{Re}_d = 273$ in the former study [6].

Furthermore, due to the higher resolution in the present simulation, variation of l_1 following the dominant second-mode oscillation is observed, which was not shown in the former study [6]. It can be shown that l_1 decreases when the drop deforms from prolate to oblate shapes, and increases when the drop returns back to the prolate shape. There exits a small time lag between the temporal variation of l_1 and e due to the inertial effect. Here e reaches the local minimum at about $(t - t_d)/\tau_{\text{osc}} = 5.44$, while l_1 does not get to the local minimum until about $(t - t_d)/\tau_{\text{osc}} = 5.58$. The distance between wake-vortex center and the top of the drop l_3 also generally increases over time similar to l_1, though the increase is more gradual. As a result, its variation within the time range shown in Fig. 15 is mainly dictated by the drop oscillation. The amplitude increase of l_2 over a cycle is also small, similar to l_3. The difference between l_2 and l_3 is that l_2 is large when the drop is oblate and is reduced when the drop turns back to the prolate shape. This is because when the drop deforms toward the oblate shape, the wake-vortex center is also pulled toward the lateral side.

D. Vortex dynamics

It is well known that streamlines are insufficient to fully identify vortices. Galilean invariant flow properties must be used instead. The swirling-strength vortex-identification criterion [54], also known as the λ_{ci} criterion, is employed here to illustrate the evolution of vortices; see Fig. 16. The λ_{ci} criterion has been shown to be an effective way to visualize vortices [54,55]. The vorticity, though it cannot fully identify the vortices as λ_{ci} (since λ_{ci} excludes the contribution from strain), is also plotted here to indicate the rotation directions of vortices. The vortex rotation directions are clockwise and counterclockwise for $\Omega < 0$ (purple color) and $\Omega > 0$ (green color) on the right half of the drop, respectively.

The figures are organized in such a way that the six rows represent the first, third, fourth, fifth, sixth, and seventh oscillations based on the dominant second mode (see Fig. 9), as reflected by the time normalized by the dominant second-mode period, $\tau_{\text{osc}} = \tau_2$.

For the first row of the figure, the drop relative velocity is small, and the effect of the falling motion is negligible. The multiple small vortices outside the drop are generated due to higher-order oscillation modes (see also the velocity field in Fig. 13). As time elapses, the amplitudes of the oscillations decrease in time due to viscous dissipation of the internal flow. It is shown in Fig. 11 that the decay rate is faster for the higher-order modes. As a result, the small vortices outside the drop disappear in the second row of Fig. 16. Only the larger vortices corresponding to the lower-order modes (e.g., $n \leqslant 3$) survive.

In the first two rows (the first three second-mode oscillations), there is no vortex seen inside the drop. As the falling velocity continues to increase, the influence of the external flow becomes stronger, and vortices inside the drop start to arise, at about the middle of third row of Fig. 16 $[(t - t_d)/\tau_{\text{osc}} \approx 3.5]$. As explained above the formation of vortices inside the drop occurs when the drop deforms from oblate to prolate shapes and is the outcome of the interaction between drop shape oscillation and the external flow. The two internal vortices near the top and the bottom rotate in different directions, as indicated by the different colors in the vorticity plots.

It can be seen from Fig. 10 that the drop Reynolds number reaches 190 at $(t - t_d)/\tau_{\text{osc}} \approx 2$, and the wake developing at the downstream side of the drop can be seen from the second row of Fig. 16. From the subsequent rows of the figure, it can be observed that the shape and relative location of the wake vortex change periodically following the dominant second-mode oscillation.

An important observation from the λ_{ci} plots is that the vortices inside the drop indeed remain even when the drop shape changes from prolate to oblate, even though they are invisible in the streamline
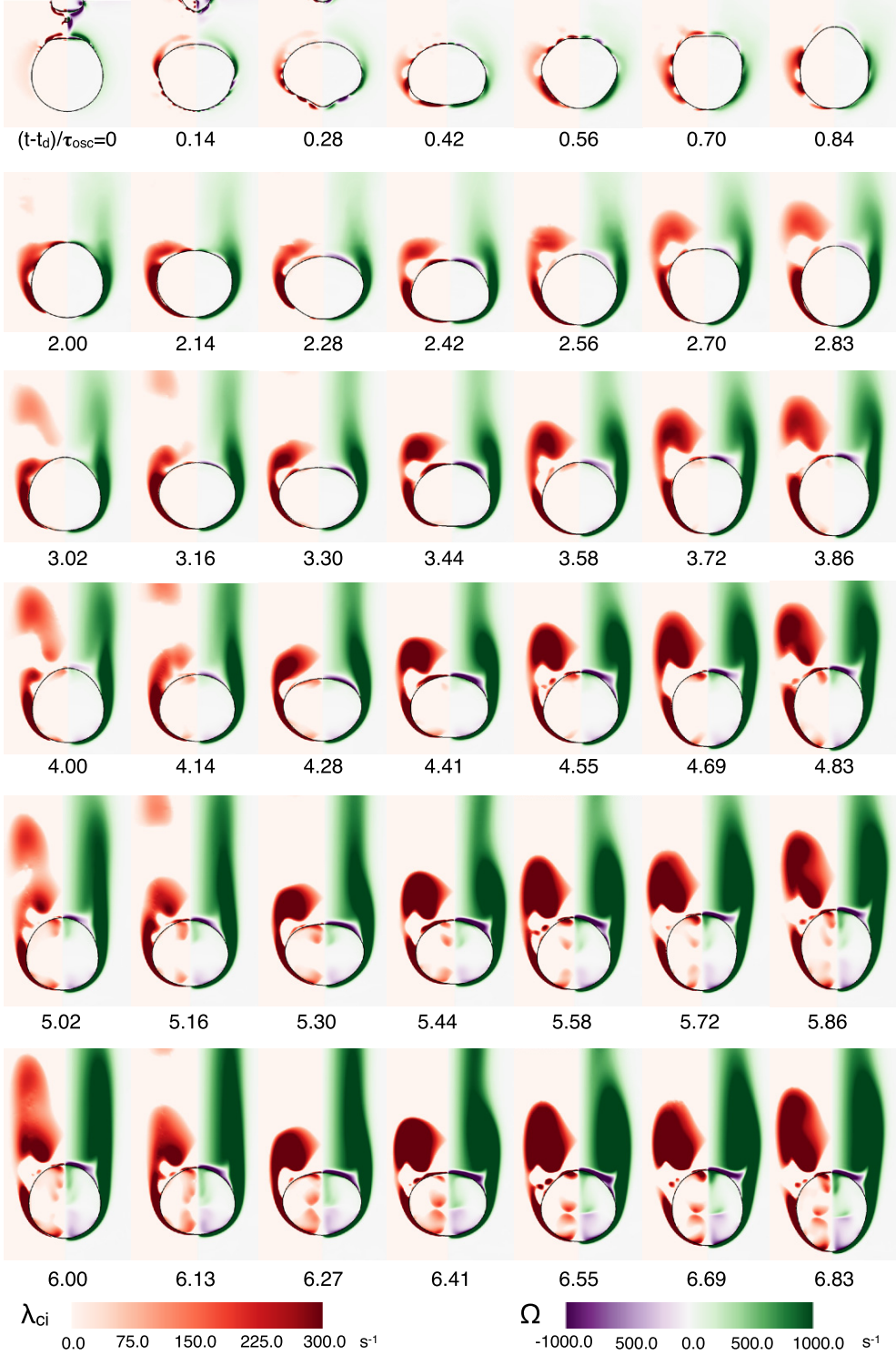
FIG. 16. Evolution of λ_{ci} (left) and vorticity (right) for the dripping drop. The vortices are visualized by the λ_{ci} criterion.
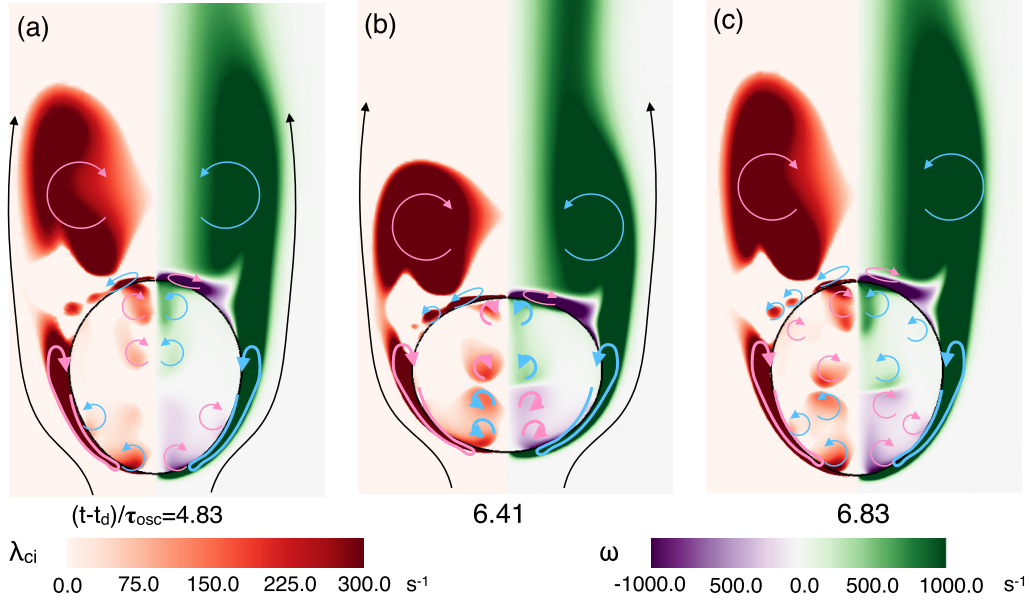
FIG. 17. Closeup of the vortices formed around the drop. Annotations are added to indicate the rotation direction.

plots as shown in Fig. 15. The potential flow induced by the prolate-to-oblate oscillation is strong and dominates the streamline pattern. Therefore, though local swirling motions exist, they can only be shown by Galilean-invariant vortex-identification scalars like λ_{ci}. From the vorticity plots, it is learned that the rotation directions of the internal vortices do not change over an oscillation cycle, even though the potential flow direction changes in the second-mode oscillation cycle; see Fig. 15. On the right half of the figure the top vortex always rotates in counterclockwise direction, while the bottom one swirls in the clockwise direction all the time.

Closeups of the vortices with annotations are shown in Fig. 17. The topology of the vortices inside the drop changes within an oscillation cycle. When the drop deforms toward the prolate shape, the vortices are stretched and can even split into two pieces. During the oblate-to-prolate deformation, the vortices at the lateral side are pushed toward the axis and will eventually merge with the ones which are already there.

E. A summary of transient flow development inside the drop

With the assistance of both the streamlines and contours of λ_{ci} and vorticity, the development of the transient flow and the vortices interaction inside the drop can be described as follows:

(1) The internal flow induced by prolate-to-oblate oscillation is aligned and enhanced by the external flow.

(2) As the falling velocity increases, at a certain point, the oblate-to-prolate deformation fails to fully reverse the internal flow induced by its prolate-to-oblate counterpart.

(3) Then a saddle point (curve) arises inside the drop when the drop deforms from its most oblate shape toward the prolate shape.

(4) The saddle point induces two vortices rotating in different directions inside the drop.

(5) As the internal circulations are different from the external flows, roller vortices are formed to satisfy kinematics.
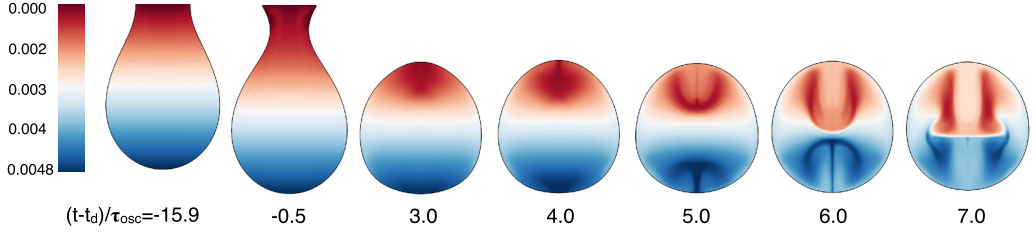
FIG. 18. Evolution of the tracer function distribution.

(6) As the drop continues to deform toward its most prolate shape, the two vortices are pushed toward the axis. (If there are vortices already near the axis, the new ones will merge with the old ones.)

(7) The vortices near the axis will be stretched and may split when the drop deforms toward the prolate shape.

(8) When the drop deforms back to the prolate shape, the two vortices remain present and the rotation directions do not change.

(9) Going back to (3) and a new cycle starts.

F. Passive scalar transport within the drop

It is of interest for many drop applications to know the influence of the transient flow within a oscillating drop on scalar transport inside the drop. The question of interest is whether mixing will occur if inhomogeneous fluids are injected into the drop through the nozzle. Although mixing of different fluids inside the drop is not the focus of the present study, here a passive tracer function is introduced in the simulation to illustrate the transport process within the drop. The initial value of the tracer function is set as the streamwise coordinate z. The evolution of the tracer field serves to reveal the accumulation effect of the transient internal flow development described above on scalar transport.

The advection equation of the tracer function is only solved within the liquid phase. The Godunov advection scheme with the second-order centered estimate for the velocity gradient was used. There exists a small numerical diffusion, but due to the fine mesh used, the numerical diffusion effect on the advection process is small. The results of the tracer function at different times are shown in Fig. 18. Before the drop detaches from the nozzle, the tracer function varies only with z. The tracer function here can be considered to mimic an imaginary experiment in which the fluid fed in the nozzle is dyed sequentially with blue, white, and red colors. When the neck of the pendant drop develops, the tracer function is redistributed by the vortex ring created by the Ventruri jet through the neck [56]. The tracer function in the lower part of the drop remains unchanged.

The snapshots of the drop after detachment are chosen to exhibit similar eccentricity, namely, similar phases in the second-mode oscillation. When the drop simply oscillates at early time $[0 < (t - t_d)/\tau_{\rm osc} < 3]$, the tracer function distribution varies only in z, similar to the initial distribution. The shape oscillation by itself may introduce longitudinal motion (for example, by the odd modes) but will not lead to net longitudinal transport of the tracer function. This is simply because the fluid motion induced by small-amplitude oscillation is symmetric, and after one oscillation cycle the scalar function distribution will return to its original state. As the falling velocity increases, the external flow develops and interacts with the drop oscillation. Vortices arise inside the drop, and they translate and interact following the drop oscillation cycle. Then stretching and folding of the fluids of different tracer function values are observed. As the top and bottom circulations are of different directions, the folding directions of the red and blue fluids are different. Though the fluids are "mixed" inside the top and bottom portions of the drop, the two portions remain segregated most of the time. At later time, however, more complex distorted patterns of the

tracer function arise, which is due to the unsteady motion of the saddle point [see Figs. 15(c)–15(f)]. If the simulation was run for a longer time to allow more oscillation cycles, chaotic mixing [57,58] of inhomogeneous fluids may arise. More detailed investigation of transport phenomena will be left for our future work.

VI. CONCLUSIONS

The short-term transient falling dynamics of a dripping water drop has been studied. One specific case with a low inflow rate in the dripping regime is considered. The focus is on the short-term behavior, and the time range considered covers about eight dominant second-mode oscillations of the drop after it is formed. A high-resolution numerical simulation has been performed to investigate the oscillation and falling dynamics. Experiments under the same conditions were also conducted for validation purposes. The grid-refinement study and the excellent agreement between simulation and experiment and theory verify and validate the simulation results. Despite the low fluid inertia, the postformation state of the drop still triggers a nonlinear oscillation. To rigorously account for the effect of drop formation on shape oscillation, the overall process including the drop growth, pinch-off, and fall has been studied. The interaction between the shape oscillation and the falling motion introduces complex oscillation dynamics and transient flow around the drop.

a. Drop formation. The experimental results for the growing pendant drop, such as the relation between drop height and volume, agree well with the static pendant drop theory, which confirms that the drop development process is quasistatic and can be fully described by the static theory. This justifies the way the simulation setup by using the static pendant drop solution slightly ahead of the pinch-off time as the initial condition in the simulation. The computed drop contours for the drop growth and formation match very well with the experimental results, validating the setup of the numerical model. Though pinching dynamics is not the focus of the present study, evolutions of the velocity and pressure fields are presented to illustrate important features for low-viscosity liquid drop formation, including the shifting of the minimum radius to the two ends of the liquid bridge, the interface overturning before pinch-off occurs, and the formation of the secondary drop. The temporal evolution of the liquid bridge minimum radius shows an initial inertial regime [$(t_d - t)^{2/3}$ power law] which later transitions to the viscous regime [$(t_d - t)^1$ linear law]. The results affirm that the drop formation is precisely captured.

b. Effect of drop formation on drop oscillation. The postformation state serves as the initial condition for the subsequent oscillation of the drop. The initial shape of the drop when it is just formed is decomposed into spherical harmonic modes. The initial mode amplitudes, characterized by the Fourier-Legendre coefficients, are found to be finite for the modes $n \leqslant 10$ considered. The pinching dynamics such as interface overturning introduces small-scale variation on the drop contour, which in turn contributes to the finite amplitudes of the higher-order modes. Furthermore, during the pinching process the high pressure in the neck expels fluids toward the to-be-formed drop, which leads to a significant downward velocity in the top region of the drop when it is just detached. The initial kinetic energy is as important as the initial surface energy contained in the drop shape and is found to amplify the initial oscillation amplitude and to induce a phase shift in the oscillation of all the modes. By incorporating both the initial surface and kinetic energy, the linear model for a free drop oscillation yields very good predictions for the second and third modes.

c. Effect of nonlinear dynamics on drop oscillation. The postformation state of the drop triggers a moderately nonlinear drop oscillation. The oscillation amplitude for the dominant second mode is about 10%, so the influence of finite amplitude on oscillation frequency is small for all the modes considered here. Nevertheless, typical nonlinear effects including asymmetry in oscillation amplitude and interaction between different modes are identified. The nonlinear effects are more profound for higher-order modes ($n \geqslant 4$) than lower-order modes ($n = 2, 3$). Since the majority of energy is stored in the lower-order modes, the small energy transfer between modes may be significant for the higher-order modes but will have little impact on the lower-order modes. Mode

coupling is clearly reflected in the frequency spectra of the Fourier-Legendre coefficients. In the spectrum of a given mode n, a primary frequency that is very similar to the Lamb frequency can be identified. Furthermore, the spectrum shows secondary frequencies corresponding to different modes due to mode coupling. Due to the low viscosity of water, there exists a commensurate relation between the $n = 2$ and 4 modes, which explains why nonlinear effects are always strongest for the $n = 4$ mode.

d. Effect of falling motion on drop oscillation. The present results indicate that the effect of the fall on the oscillation frequency is little for the time range considered here. The oscillation frequency for the falling drop agrees well with Lamb's prediction even when the drop Reynolds number exceeds the oscillation Reynolds number for 75%. This conclusion is true for both lower and higher order modes. The effect of the drop fall on shape oscillation lies mainly in the time evolution of the amplitudes of the various shape oscillation modes. The increasing shear stress induced by the falling motion changes the force balance with surface tension, resulting in a strengthened upward shift in oscillation amplitude for the higher-order even modes. The drop falling motion also seems to provide energy to the oscillations, and as a result, the damping in amplitude is slowed down for $(t - t_d)/\tau_{osc} \gtrsim 4$.

e. Effect of drop oscillation on transient flow development. When the drop falls without oscillation, the external shear induced by the falling motion will induce the Hill vortex within the drop. For the present case, nonlinear shape oscillation interacts with the external flow induced by the falling motion, resulting in a complicated transient flow around the drop. When the drop oscillates from prolate to oblate shapes, the flow induced by the oscillation is aligned with the external flow. In contrast, for a oblate-to-prolate deformation, the flow goes against the external flow. As a result, a saddle point (curve for the axisymmetric geometry) arises in the drop, which gives rise to two counterrotating vortices. The rotating directions of the vortices remain unchanged, while the potential flow directions vary due to the dominant second-mode oscillation. The drop oscillation also influences the wake geometry. The swirling-strength vortex-identification criterion (λ_{ci}) and the vorticity are employed to better elucidate the vortex dynamics. When the drop oscillates, the vortices inside can be stretched and even split. Finally, a tracer function is introduced to demonstrate the scalar transport within the drop. Pure shape oscillation does not induce net longitudinal transport of the tracer function. Stretching and folding of the scalar function contours are only observed after vortices arise within the drop. The unsteady motion of the saddle point creates a more distorted tracer function field, which may result in a chaotic mixing of inhomogeneous fluids inside the drop. Yet a longer simulation than the present one will be required to fully verify this.

ACKNOWLEDGMENTS

APPENDIX A: PENDANT DROP THEORY

The shape of a static pendant drop can be calculated based on the equilibrium equation [7],

$$\sigma \left(\frac{1}{\mathcal{R}_1} + \frac{1}{\mathcal{R}_2} \right) = 2\sigma \kappa_b - (\rho_l - \rho_g)gz', \tag{A1}$$
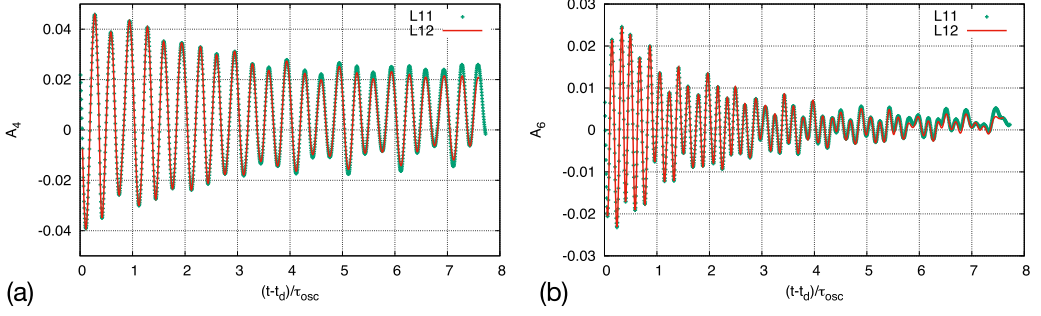
FIG. 19. Temporal evolutions of the Fourier-Legendre coefficients for the (a) $n = 4$ and (b) $n = 6$ modes for different mesh resolutions.

where ρ_l and ρ_g are the water and air densities respectively and κ_b is the curvature at the bottom of the pendant drop. The two principal radii of curvature, $\mathcal{R}_1$ and $\mathcal{R}_2$, can be calculated as

$$\frac{1}{\mathcal{R}_1} = \frac{\partial \phi}{\partial s}, \quad \frac{1}{\mathcal{R}_2} = \frac{\sin \phi}{x'}, \tag{A2}$$

where s is the curvilinear coordinate starting from the bottom of the drop; see Fig. 4. Then Eq. (A1) can be written as

$$\frac{\partial \phi}{\partial s} = 2\kappa_b - \frac{(\rho_l - \rho_g)gz'}{\sigma} - \frac{\sin \phi}{x'}. \tag{A3}$$

It can also be shown from geometry that

$$\frac{\partial x'}{\partial s} = \cos \phi, \tag{A4}$$

$$\frac{\partial z'}{\partial s} = \sin \phi. \tag{A5}$$

At the end the ODE system, Eqs. (A3), (A4), and (A5), can be solved numerically to yield the contour of the static pendant drop.

APPENDIX B: GRID INDEPENDENCE STUDY FOR THE EVOLUTION OF THE AMPLITUDE OF SPHERICAL HARMONIC MODES

To fully confirm the results of Fourier-Legendre coefficients shown in Fig. 11 are grid independent, a simulation with an additional refinement level $L = 12$ has been performed. The results for the $n = 4$ and 6 modes are shown in Fig. 19, confirming that the important conclusions made related to the effect of drop formation, nonlinear dynamics, and falling motion on the drop oscillation are independent of the grid resolution.

---

[1] J. Q. Feng and K. V. Beard, A perturbation model of raindrop oscillation characteristics with aerodynamic effects, J. Atmos. Sci. **48**, 1856 (1991).

[2] O. A. Basaran, H. Gao, and P. P. Bhat, Nonstandard inkjets, Annu. Rev. Fluid Mech. **45**, 85 (2013).

[3] C. Clanet and J. C. Lasheras, Transition from dripping to jetting, J. Fluid Mech. **383**, 307 (1999).

[4] B. Lalanne, S. Tanguy, and F. Risso, Effect of rising motion on the damped shape oscillations of drops and bubbles, Phys. Fluids **25**, 112107 (2013).

[5] M. Agrawal, A. R. Premlata, M. K. Tripathi, B. Karri, and K. C. Sahu, Nonspherical liquid droplet falling in air, Phys. Rev. E **95**, 033111 (2017).

[6] K. Bergeles, Y. Hardalupas, and A. M. K. P. Taylor, On the transient flow inside and around a deforming millimetre class oil droplet falling under the action of gravity in stagnant air, Phys. Fluids **30**, 013305 (2018).

[7] J. F. Padday and A. R. Pitt, The stability of axisymmetric menisci, Philos. Trans. R. Soc. London A **275**, 489 (1973).

[8] P. T. Sumesh and R. Govindarajan, The possible equilibrium shapes of static pendant drops, J. Chem. Phys. **133**, 144707 (2010).

[9] R. M. S. M. Schulkes, The evolution and bifurcation of a pendant drop, J. Fluid Mech. **278**, 83 (1994).

[10] P. Coullet, L. Mahadevan, and C. S. Riera, Hydrodynamical models for the chaotic dripping faucet, J. Fluid Mech. **526**, 1 (2005).

[11] J. R. Castrejón-Pita, A. A. Castrejón-Pita, S. S. Thete, K. Sambath, I. M. Hutchings, J. Hinch, J. R. Lister, and O. A. Basaran, Plethora of transitions during breakup of liquid filaments, Proc. Natl. Acad. Sci. USA **112**, 4582 (2015).

[12] J. Eggers, Universal Pinching of 3D Axisymmetric Free-Surface Flow, Phys. Rev. Lett. **71**, 3458 (1993).

[13] J. Eggers and T. F. Dupont, Drop formation in a one-dimensional approximation of the Navier–Stokes equation, J. Fluid Mech. **262**, 205 (1994).

[14] D. T. Papageorgiou, On the breakup of viscous liquid threads, Phys. Fluids **7**, 1529 (1995).

[15] R. F. Day, E. J. Hinch, and J. R. Lister, Self-Similar Capillary Pinchoff of an Inviscid Fluid, Phys. Rev. Lett. **80**, 704 (1998).

[16] B. W. Zeff, B. Kleber, J. Fineberg, and D. P. Lathrop, Singularity dynamics in curvature collapse and jet eruption on a fluid surface, Nature (London) **403**, 401 (2000).

[17] A. U. Chen, P. K. Notz, and O. A. Basaran, Computational and Experimental Analysis of Pinch-Off and Scaling, Phys. Rev. Lett. **88**, 174501 (2002).

[18] P. Doshi, I. Cohen, W. W. Zhang, M. Siegel, P. Howell, O. A. Basaran, and S. R. Nagel, Persistence of memory in drop breakup: The breakdown of universality, Science **302**, 1185 (2003).

[19] J. R. Castrejon-Pita, A. A. Castrejon-Pita, E. J. Hinch, J. R. Lister, and I. M. Hutchings, Self-similar breakup of near-inviscid liquids, Phys. Rev. E **86**, 015301(R) (2012).

[20] E. D. Wilkes, S. D. Phillips, and O. A. Basaran, Computational and experimental analysis of dynamics of drop formation, Phys. Fluids **11**, 3577 (1999).

[21] A. van der Bos, M.-J. van der Meulen, T. Driessen, M. van den Berg, H. Reinten, H. Wijshoff, M. Versluis, and D. Lohse, Velocity Profile Inside Piezoacoustic Inkjet Droplets in Flight: Comparison Between Experiment and Numerical Simulation, Phys. Rev. Applied **1**, 014004 (2014).

[22] M. P. Borthakur, G. Biswas, and D. Bandyopadhyay, Formation of liquid drops at an orifice and dynamics of pinch-off in liquid jets, Phys. Rev. E **96**, 013115 (2017).

[23] X. Zhang, Dynamics of drop formation in viscous flows, Chem. Eng. Sci. **54**, 1759 (1999).

[24] L. Rayleigh, On the capillary phenomena of jets, Proc. R. Soc. London **29**, 71 (1879).

[25] H. Lamb, *Hydrodynamics* (Cambridge University Press, Cambridge, 1932).

[26] W. H. Reid, The oscillations of a viscous liquid drop, Q. Appl. Math. **18**, 86 (1960).

[27] C. A. Miller and L. E. Scriven, The oscillations of a fluid droplet immersed in another fluid, J. Fluid Mech. **32**, 417 (1968).

[28] A. Prosperetti, Normal-mode analysis for the oscillations of a viscous-liquid drop in an immiscible liquid, J. Méc. **19**, 149 (1980).

[29] J. A. Tsamopoulos and R. A. Brown, Nonlinear oscillations of inviscid drops and bubbles, J. Fluid Mech. **127**, 519 (1983).

[30] R. Natarajan and R. A. Brown, Third-order resonance effects and the nonlinear stability of drop oscillations, J. Fluid Mech. **183**, 95 (1987).

[31] E. Becker, W. J. Hiller, and T. A. Kowalewski, Experimental and theoretical investigation of large-amplitude oscillations of liquid droplets, J. Fluid Mech. **231**, 189 (1991).

[32] O. A. Basaran, Nonlinear oscillations of viscous liquid drops, J. Fluid Mech. **241**, 169 (1992).

[33] E. Becker, W. J. Hiller, and T. A. Kowalewski, Nonlinear dynamics of viscous droplets, J. Fluid Mech. **258**, 191 (1994).

[34] D. J. Gunn, Transfer of heat or mass to particles in fixed and fluidised beds, Int. J. Heat Mass Transfer **21**, 467 (1978).

[35] B. T. Helenbrook and C. F. Edwards, Quasi-steady deformation and drag of uncontaminated liquid drops, Int. J. Multiphase Flow **28**, 1631 (2002).

[36] J. Q. Feng, A deformable liquid drop falling through a quiescent gas at terminal velocity, J. Fluid Mech. **658**, 438 (2010).

[37] H. J. J. Staat, A. van der Bos, M. van den Berg, H. Reinten, H. Wijshoff, M. Versluis, and D. Lohse, Ultrafast imaging method to measure surface tension and viscosity of inkjet-printed droplets in flight, Exp. Fluids **58**, 2 (2017).

[38] M. K. Tripathi, K. C. Sahu, and R. Govindarajan, Why a falling drop does not in general behave like a rising bubble, Sci. Rep. **4**, 4771 (2014).

[39] P. Ern, F. Risso, D. Fabre, and J. Magnaudet, Wake-induced oscillatory paths of bodies freely rising or falling in fluids, Annu. Rev. Fluid Mech. **44**, 97 (2012).

[40] S. K. Chung and E. H. Trinh, Internal flow of an electrostatically levitated droplet undergoing resonant shape oscillation, Phys. Fluids **12**, 249 (2000).

[41] G. Tryggvason, R. Scardovelli, and S. Zaleski, *Direct Numerical Simulations of Gas-Liquid Multiphase Flows* (Cambridge University Press, Cambridge, 2011).

[42] X. Zhang, Dynamics of growth and breakup of viscous pendant drops into air, J. Colloid Interface Sci. **212**, 107 (1999).

[43] D. Gueyffier, J. Li, A. Nadim, R. Scardovelli, and S. Zaleski, Volume-of-fluid interface tracking with smoothed surface stress methods for three-dimensional flows, J. Comput. Phys. **152**, 423 (1999).

[44] H. Deka, B. Ray, G. Biswas, A. Dalal, P.-H. Tsai, and A.-B. Wang, The regime of large bubble entrapment during a single drop impact on a liquid pool, Phys. Fluids **29**, 092101 (2017).

[45] R. Gunn and G. D. Kinzer, The terminal velocity of fall for water droplets in stagnant air, J. Meteorol. **6**, 243 (1949).

[46] S. Popinet, Gerris: A tree-based adaptive solver for the incompressible Euler equations in complex geometries, J. Comput. Phys. **190**, 572 (2003).

[47] S. Popinet, An accurate adaptive solver for surface-tension-driven interfacial flows, J. Comput. Phys. **228**, 5838 (2009).

[48] R. Scardovelli and S. Zaleski, Direct numerical simulation of free-surface and interfacial flow, Annu. Rev. Fluid Mech. **31**, 567 (1999).

[49] M. M. Francois, S. J. Cummins, E. D. Dendy, D. B. Kothe, J. M. Sicilian, and M. W. Williams, A balanced-force algorithm for continuous and sharp interfacial surface tension models within a volume tracking framework, J. Comput. Phys. **213**, 141 (2006).

[50] B. Ambravaneswaran, E. D. Wilkes, and O. A. Basaran, Drop formation from a capillary tube: Comparison of one-dimensional and two-dimensional analyses and occurrence of satellite drops, Phys. Fluids **14**, 2606 (2002).

[51] X. Zhang and O. A. Basaran, An experimental study of dynamics of drop formation, Phys. Fluids **7**, 1184 (1995).

[52] Y. Ling, J.-M. Fullana, S. Popinet, and C. Josserand, Droplet migration in a Hele–Shaw cell: Effect of the lubrication film on the droplet dynamics, Phys. Fluids **28**, 062001 (2016).

[53] M. J. M. Hill, On a spherical vortex, Philos. Trans. R. Soc. London A **185**, 213 (1894).

[54] J. Zhou, R. J. Adrian, S. Balachandar, and T. M. Kendall, Mechanisms for generating coherent packets of hairpin vortices in channel flow, J. Fluid Mech. **387**, 353 (1999).

[55] P. Chakraborty, S. Balachandar, and R. J. Adrian, On the relationships between local vortex identification schemes, J. Fluid Mech. **535**, 189 (2005).

[56] J. Hoepffner and G. Paré, Recoil of a liquid filament: Escape from pinch-off through creation of a vortex ring, J. Fluid Mech. **734**, 183 (2013).

[57] H. Aref and S. Balachandar, Chaotic advection in a Stokes flow, Phys. Fluids **29**, 3515 (1986).

[58] J. R. Angilella and J. P. Brancher, Note on chaotic advection in an oscillating drop, Phys. Fluids **15**, 261 (2003).